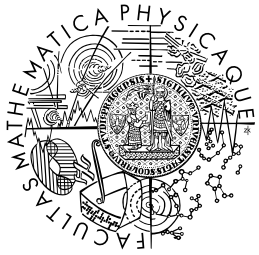

FACULTY
OF MATHEMATICS
AND PHYSICS
Charles University

BACHELOR THESIS

Aleš Melzer

Magneto-optical studies of the influence of buffer layer on magnetic properties of $La_{2/3}Sr_{1/3}MnO_3$ thin films

Institute of Physics of Charles University

Supervisor of the bachelor thesis: RNDr. Martin Veis, Ph.D.

Study programme: Physics

Study branch: Physics

Prague 2023

I declare that I carried out this bachelor thesis independently, and only with the cited sources, literature and other professional sources. It has not been used to obtain another or the same degree.

I understand that my work relates to the rights and obligations under the Act No. 121/2000 Sb., the Copyright Act, as amended, in particular the fact that the Charles University has the right to conclude a license agreement on the use of this work as a school work pursuant to Section 60 subsection 1 of the Copyright Act.

In ..... date ....

Author's signature

I would like to thank my supervisor RNDr. Martin Veis, Ph.D. and my advisor Mgr. Tomáš Maleček for their invaluable guidance and support, as it is what made this work possible.

Title: Magneto-optical studies of the influence of buffer layer on magnetic properties of $La_{2/3}Sr_{1/3}MnO_3$ thin films

Author: Aleš Melzer

Institute: Institute of Physics of Charles University

Supervisor: RNDr. Martin Veis, Ph.D., Institute of Physics of Charles University

Abstract: The impact of film thickness on optical and magneto-optical properties of $La_{2/3}Sr_{1/3}O_3$ (LSMO) thin films was studied by optical and magneto-optical methods. A series of LSMO samples with increasing thicknesses was prepared by pulsed laser deposition on a silicon substrate with a $Ca_2Nb_3O_{10}$ seed layer. The topology of both the substrates and the deposited films was examined by atomic force microscopy. The samples were subsequently analysed by spectroscopic ellipsometry and magneto-optical spectroscopy. The off-diagonal elements of the permittivity tensor of each layer were afterwards determined numerically from these measurements. The obtained spectra exhibited spectroscopic structures found in epitaxial LSMO films grown on $SrTiO_3$ (STO), reflecting good crystalline quality of investigated samples. Effects related to gradual strain relaxation with increasing film thickness were observed on the spectra.

Keywords: Magneto-optical Kerr effect, $Ca_2Nb_3O_{10}$ nanosheets

Contents

Introduction **3**

1 Electromagnetic waves **5**
1.1 Wave equation 5
1.2 Plane wave 6

2 Polarisation of light **7**
2.1 Polarisation 7
2.2 Jones calculus 10
2.2.1 Jones vector 10
2.2.2 Jones matrix 12
2.3 Complex polarisation parameter 14
2.4 Magneto-optical observables 15

3 Optically anisotropic media **17**
3.1 Permittivity tensor 17
3.2 Yeh formalism 19

4 Experimental techniques **25**
4.1 Pulsed laser deposition 25
4.2 Atomic force microscopy 26
4.3 Spectroscopic ellipsometry 27
4.4 Magneto-optical spectroscopy 29

5 Structural and magnetic properties of $La_{2/3}Sr_{1/3}MnO_3$ **32**
5.1 Structure of bulk LSMO 32
5.2 Ferromagnetism 33
5.3 Magnetic properties of LSMO 34

6 Investigated samples **36**
6.1 Thin film LSMO 36
6.2 $Ca_2Nb_3O_{10}$ nanosheets 37
6.3 LSMO/NS/Si thin films 38
6.4 Investigated LSMO/NS/Si films 38

7 Permittivity tensor element spectra of investigated samples **40**
7.1 Diagonal elements of the permittivity tensor 40
7.2 MO Kerr effect 42
7.3 Off-diagonal elements of the permittivity tensor 44

Conclusion **47**

Bibliography **48**

List of Abbreviations **52**

A Supplementary graphs **53**
A.1 Diagonal elements of the permittivity tensors of selected materials 53
A.2 100 nm LSMO/NS/Si absorption coefficient 55
A.3 Simulated MOKE of the 100 nm sample 56

Introduction

In this thesis, we thoroughly analyse the development of optical and magneto-optical properties in $La_{2/3}Sr_{1/3}MnO_3$ thin films grown on silicon with the use of a 2D nanosheet buffer layer.

Hole-doped manganites $La_{1-x}M_xMnO_3$, where M stands for either Ca, Sr, or Ba, garner attention from the wide scientific community due to their extraordinary set of physical properties. The most notable pair of properties shared throughout the whole family of hole-doped manganites is colossal magnetoresistance (CMR) [1] combined with a high degree of spin polarisation. The particular case of $La_{2/3}Sr_{1/3}MnO_3$ (LSMO) has been studied extensively due to its very high Curie temperature ($T_C \sim 370$ K [2]) and nearly 100% spin polarisation [3]. These physical properties make LSMO suitable for application not only in the field of spintronics but also sensor [4] and fuel cell development [5].

The origin of ferromagnetic ordering in LSMO lies in the presence of mixed valence manganese ions Mn^{3+} and Mn^{4+}. These manganese ions can exchange an e_g electron via the O^{2-} 2p state while preserving its spin. This was dubbed the double-exchange (DE) interaction and was first explained by C. Zener in [6]. The probability of the DE interaction is heavily dependent on the geometry of Mn^{3+}–O–Mn^{4+}. Hence the rotation and distortion of the MnO_6 octahedra inside the crystalline structure of LSMO play an essential role in forming its magnetic properties. The geometry of the MnO_6 octahedra is influenced by epitaxial strain caused by lattice mismatch and by coupling of the octahedral rotations at the sample-substrate interface [7].

LSMO is conventionally grown epitaxially on single-crystal oxide substrates such as $SrTiO_3$ (STO) due to the large dependence of LSMO's properties on the quality of its crystalline structure. Being able to grow thin LSMO films of similar crystalline quality on low-cost substrates such as Si would prove beneficial for future wide-scale industrial adaptation. However, growing LSMO directly on Si results in polycrystalline films suffering from a major degradation of LSMO's sought-after properties [8].

This study explores the use of $Ca_2Nb_3O_{10}$ (CNO) nanosheets (NS) as a buffer layer between Si and LSMO to facilitate locally epitaxial growth of the LSMO film. The two-dimensional CNO nanosheet lattice has a square a-b plane with a lattice parameter of $a_{\mathrm{NS}} = 0.386$ nm giving a lattice mismatch with LSMO of -0.18 %. Growing LSMO on a NS/Si substrate results in a (001)-textured film [9] with properties similar to films grown on conventional substrates while also benefiting from properties found in polycrystalline films, such as low-field magnetoresistance [8].

This thesis begins by introducing the electromagnetic plane wave as a solution to the wave equation. In the second chapter, the polarisation of light is discussed as an innate property of electromagnetic plane waves. An overview of Jones calculus is also encompassed in the second chapter as a way to describe the polarisation state of fully polarised light. The permittivity tensor characterising anisotropic media is presented in the third chapter. It is subsequently used in the derivation of the magneto-optical response of investigated samples by means of Yeh formalism. The fourth chapter makes use of the theory introduced thus far to acquaint the reader with the experimental methods used in this work. Chapters five and six shift focus to analysed samples. Chapter five begins by showcasing the properties of bulk LSMO and gradually progresses into chapter six, which serves as the introduction of thin film LSMO, CNO nanosheets and deposited LSMO/NS/Si samples. The final chapter, chapter seven, encapsulates the results of the carried-out research.

Chapter 1

Electromagnetic waves

Experimental methods used in this thesis depend on studying the interaction of visible light with the investigated samples. Visible light consists of electromagnetic waves in a specific frequency range. This chapter will derive the wave equation from the fundamental principles of electromagnetism – the Maxwell Equations and demonstrate the plane wave as a solution to a special case of an electromagnetic wave propagating through a vacuum.

1.1 Wave equation

The aforementioned Maxwell equations are a set of universally applicable differential relations linking together the electric field $\mathbf{E}$, magnetic induction $\mathbf{B}$, the displacement field $\mathbf{D}$, magnetic field $\mathbf{H}$, free current density $\mathbf{j_f}$ and free charge density ρ_f [10]

$$\boldsymbol{\nabla} \times \mathbf{E} + \frac{\partial \mathbf{B}}{\partial t} = 0 \,, \tag{1.1}$$

$$\boldsymbol{\nabla} \cdot \mathbf{B} = 0 \,, \tag{1.2}$$

$$\boldsymbol{\nabla} \times \mathbf{H} - \frac{\partial \mathbf{D}}{\partial t} = \mathbf{j_f} \,, \tag{1.3}$$

$$\boldsymbol{\nabla} \cdot \mathbf{D} = \rho_f \,. \tag{1.4}$$

The following derivation will assume a material abiding by the constitutive relations and Ohm's law. The constitutive relations are used to model the behaviour of materials subjected to electromagnetic fields. Constitutive relation 1.5 sets linear relationships between elements of $\mathbf{D}$ and $\mathbf{E}$ using the relative permittivity tensor $\boldsymbol{\varepsilon}$ and the permittivity of vacuum ε_0. An analogous relation 1.6 between $\mathbf{B}$ and $\mathbf{H}$ is set with the permeability tensor $\boldsymbol{\mu}$ and the permeability of vacuum μ_0. Ohm's law 1.7 sets a similar relation between free current density $\mathbf{j_f}$ and $\mathbf{E}$ utilising the conductivity tensor $\boldsymbol{\sigma}$

$$\mathbf{D} = \varepsilon_0 \boldsymbol{\varepsilon} \mathbf{E} \,, \tag{1.5}$$

$$\mathbf{B} = \mu_0 \boldsymbol{\mu} \mathbf{H} \,, \tag{1.6}$$

$$\mathbf{j_f} = \boldsymbol{\sigma} \mathbf{E} \,. \tag{1.7}$$

Any other non-linear effects are not accounted for as they are negligible in weak fields. Furthermore a static medium is assumed, therefore ε, μ, σ are assumed to be time-independent. Finally, we assume μ to be approximately 1 due to light's negligible magnetic interaction with materials at optical frequencies [11], which can be derived from light's small effect on the spin of electrons [12] as well as light's weak influence on orbiting electrons due to the Lorenz force.

Substituting the constitutive relation 1.6 into the second Maxwell equation 1.2 and the constitutive relations 1.5,1.7 into the third Maxwell equation 1.3 yields

$$\frac{1}{\mu_0}\boldsymbol{\nabla} \times \mathbf{E} + \frac{\partial \mathbf{H}}{\partial t} = 0 \,, \tag{1.8}$$

$$\boldsymbol{\nabla} \times \mathbf{H} - \varepsilon_0 \boldsymbol{\varepsilon} \frac{\partial \mathbf{E}}{\partial t} - \boldsymbol{\sigma}\mathbf{E} = 0 \,. \tag{1.9}$$

Taking the curl of 1.8 and the partial time derivative of 1.9 we get

$$\boldsymbol{\nabla} \times \left(\frac{1}{\mu_0}\boldsymbol{\nabla} \times \mathbf{E}\right) + \frac{\partial}{\partial t}\boldsymbol{\nabla} \times \mathbf{H} = 0 \,, \tag{1.10}$$

$$\frac{\partial}{\partial t}\boldsymbol{\nabla} \times \mathbf{H} - \varepsilon_0 \boldsymbol{\varepsilon} \frac{\partial^2 \mathbf{E}}{\partial t^2} - \boldsymbol{\sigma}\frac{\partial \mathbf{E}}{\partial t} = 0 \,. \tag{1.11}$$

Lastly, substituting 1.11 into 1.10 and applying the curl of a curl of a vector field identity, we reach the final electromagnetic wave equation

$$\Delta\mathbf{E} - \varepsilon_0\mu_0\boldsymbol{\varepsilon}\frac{\partial^2 \mathbf{E}}{\partial t^2} - \mu_0\boldsymbol{\sigma}\frac{\partial \mathbf{E}}{\partial t} - \nabla(\boldsymbol{\nabla} \cdot \mathbf{E}) = 0 \,. \tag{1.12}$$

1.2 Plane wave

The plane wave arises as a solution to 1.12 in the case of an electromagnetic wave propagating through an isotropic, homogeneous, non-conductive medium without any free currents or free charges. Under these additional assumptions 1.12 in a vacuum reduces to

$$\Delta\mathbf{E} - \varepsilon_0\mu_0\boldsymbol{\varepsilon}\frac{\partial^2 \mathbf{E}}{\partial t^2} = 0 \,. \tag{1.13}$$

The speed of light in vacuum $c = 1/\sqrt{\mu_0\varepsilon_0}$ is then derived by comparison with the general wave equation.

Suppose a plane wave travelling in the direction of a unit vector s. Its wavefront is then defined as a locus of points placed at r satisfying r · s = constant. Such a wave naturally abides by $\mathbf{E}(\mathbf{r}, t) = \mathbf{E}(\mathbf{r} \cdot \mathrm{s}, t)$. The monochromatic time-harmonic plane wave

$$\mathbf{E}(\mathbf{r}, t) = \mathbf{E_0}\cos(\omega t - \mathbf{k} \cdot \mathbf{r} + \delta) = \mathrm{Re}\Big\{\mathbf{E_0}e^{i(\omega t - \mathbf{k}\cdot\mathbf{r} + \delta)}\Big\} \,, \tag{1.14}$$

where $\mathbf{E_0}$, ω, k, δ stands for the amplitude of the wave, angular frequency, wavevector and phase shift, respectively, is a solution to the vacuum wave equation 1.13. This specific solution shall be used to describe the propagation of light in further chapters of this work.

Chapter 2

Polarisation of light

The previous chapter established the plane wave as a solution to the vacuum wave equation 1.13. This chapter will define polarisation of light resulting from the transversal nature of plane waves. This chapter will also cover mathematical formalisms commonly used to describe the polarisation state of monochromatic time-harmonic plane waves and its changes caused by such waves interacting with different optical elements.

2.1 Polarisation

Polarisation is a property of transversal waves stemming from the geometrical orientation of the oscillations of the electric field vector **E**. It can be shown that a wave given by 1.14 can oscillate in any direction perpendicular to the direction of propagation.

Suppose a monochromatic time-harmonic plane wave propagating along the z axis. The oscillations of the electric field **E**, perpendicular to the z axis, can be without any loss of generality expressed as a linear combination of two monochromatic time-harmonic plane waves with the same frequency. Let us denote the components oscillating along the x and y axes E_x and E_y, respectively. The components of $\mathbf{E}(z,t)$ can be then written as

$$E_x(z,t) = E_{0x}\cos(\omega t - kz + \delta_x)\ , \tag{2.1}$$

$$E_y(z,t) = E_{0y}\cos(\omega t - kz + \delta_y)\ , \tag{2.2}$$

$$E_z = 0\ , \tag{2.3}$$

where E_{0x}, E_{0y} are the positive amplitudes of the corresponding components with δ_x and δ_y being their phase offsets. It can be shown that the vector **E**(z,t) traces an ellipse as the wave propagates.

Let us define $\varphi := \omega t - kz$. Then 2.1 and 2.2 divided by their corresponding amplitudes E_{0x}, E_{0y} become

$$\frac{E_x}{E_{0x}} = \cos(\varphi + \delta_x) = \cos(\varphi)\cos(\delta_x) - \sin(\varphi)\sin(\delta_x) \ , \tag{2.4}$$

$$\frac{E_y}{E_{0y}} = \cos(\varphi + \delta_y) = \cos(\varphi)\cos(\delta_y) - \sin(\varphi)\sin(\delta_y) \ . \tag{2.5}$$

Multiplying 2.4, 2.5 by $\sin(\delta_y)$ and $\sin(\delta_x)$, respectively gives

$$\frac{E_x}{E_{0x}}\sin(\delta_y) = \cos(\varphi)\cos(\delta_x)\sin(\delta_y) - \sin(\varphi)\sin(\delta_x)\sin(\delta_y) \ , \tag{2.6}$$

$$\frac{E_y}{E_{0y}}\sin(\delta_x) = \cos(\varphi)\cos(\delta_y)\sin(\delta_x) - \sin(\varphi)\sin(\delta_y)\sin(\delta_x) \ . \tag{2.7}$$

Taking the difference of 2.6 and 2.7 causes one of the terms on the right to cancel out, leaving

$$\begin{aligned} \frac{E_x}{E_{0x}}\sin(\delta_y) - \frac{E_y}{E_{0y}}\sin(\delta_x) &= \cos(\varphi)(\cos(\delta_x)\sin(\delta_y) - \cos(\delta_y)\sin(\delta_x)) \\ &= \cos(\varphi)\sin(\delta_y - \delta_x) \ . \end{aligned} \tag{2.8}$$

Going through a similar procedure except multiplying 2.4, 2.5 by $\cos(\delta_y)$ and $\cos(\delta_x)$, respectively, and taking their difference we arrive at

$$\begin{aligned} \frac{E_x}{E_{0x}}\cos(\delta_y) - \frac{E_y}{E_{0y}}\cos(\delta_x) &= \sin(\varphi)(\sin(\delta_y)\cos(\delta_x) - \sin(\delta_x)\cos(\delta_y)) \\ &= \sin(\varphi)\sin(\delta_y - \delta_x) \ . \end{aligned} \tag{2.9}$$

Let $\delta := \delta_y - \delta_x$ be the phase difference. Taking the sum of squares of 2.8 and 2.9 finally yields

$$\left(\frac{E_x}{E_{0x}}\right)^2 - 2\frac{E_x}{E_{0x}}\frac{E_y}{E_{0y}}\cos(\delta) + \left(\frac{E_y}{E_{0y}}\right)^2 = \sin^2(\delta) \ . \tag{2.10}$$

The above formula 2.10 describes an ellipse in the plane perpendicular to the z axis, hence in the general case, the vector E traces an ellipse in the plane perpendicular to the direction of wave propagation. This ellipse is commonly referred to as the ellipse of polarisation, which can be completely described by the following four parameters:

- The *azimuth* θ - an oriented angle between the positive semi axis x and the major axis of the ellipse. This angle describes the geometrical orientation of the ellipse of polarisation and can take values from $-\pi/2$ to $\pi/2$.

- The *ellipticity angle* ϵ - determines the degree to which the polarisation ellipse deviates from being circular. Its sign is a matter of convention and is used to indicate the handedness of the electric field vector's rotation against the direction of wave propagation. In this thesis, a positive ellipticity angle represents right-handed polarisation, where the electric field vector **E** rotates clockwise along the polarisation ellipse. A negative ellipticity angle represents left-handed polarisation, with the electric field vector rotating counterclockwise. The ellipticity angle can range between $-\pi/4$ and $\pi/4$. Ellipticity e is often defined as the tangent of the ellipticity angle, given by $e = \tan\epsilon = \pm b/a$, where a is the major semi-axis and b is the minor semi-axis.
- The *amplitude* E_0 - a parameter related to the overall wave intensity as $I \approx E_0^2 = a^2 + b^2 = E_{0x}^2 + E_{0y}^2$.
- The *absolute phase* δ_0 - an oriented angle between the vector of electric intensity **E** and the positive semi axis x at $t = 0$. It only specifies the initial state and can range between $-\pi$ and π.

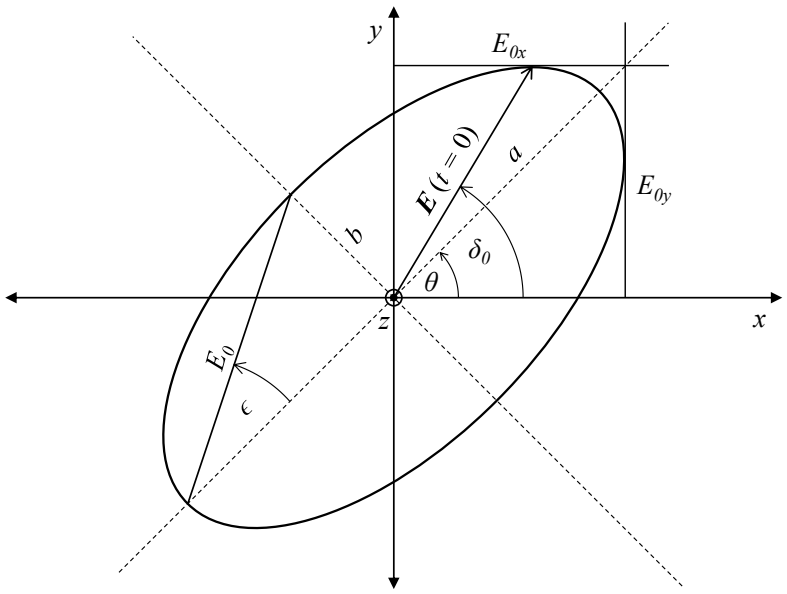

Figure 2.1 The ellipse of polarisation of a wave travelling towards the reader.

Albeit all four parameters are required to fully determine the position of $\mathbf{E}(z,t)$ for every pair of z and t, some parameters are more integral to describing the polarisation state than others. Namely, the azimuth θ and ellipticity angle ϵ hold information about the shape and orientation of the resulting ellipse, whereas the amplitude E_0 pertains to the overall light intensity and the absolute phase describes only the initial state.

It is important to note that despite all monochromatic time-harmonic plane waves being polarised, this does not hold true for polychromatic light. Light can also be only partially polarised or completely unpolarised. Partially polarised light changes its polarisation state after random intervals of time. The length of this interval approaches zero for randomly polarised light, which is commonly referred to as unpolarised light.

2.2 Jones calculus

Jones calculus is a widely used mathematical formalism capable of describing only fully polarised light. While there exist other more versatile formalisms able to describe partially polarised light as well, Jones calculus will suffice in a laboratory environment where the polarisation state of light is easily controlled.

2.2.1 Jones vector

The Jones vector is the main building block of Jones calculus. The superposition of two orthogonal monochromatic plane waves 2.1, 2.2 can be vectorised and rewritten with the use of complex amplitude defined as $A_i = E_{0i}e^{i\delta_i}$ like so

$$\mathbf{E}(z,t) = \begin{bmatrix} \mathrm{Re}\left\{E_{0x}e^{i(\omega t - kz + \delta_x)}\right\} \\ \mathrm{Re}\left\{E_{0y}e^{i(\omega t - kz + \delta_y)}\right\} \end{bmatrix} = \begin{bmatrix} \mathrm{Re}\left\{A_x e^{i(\omega t - kz)}\right\} \\ \mathrm{Re}\left\{A_y e^{i(\omega t - kz)}\right\} \end{bmatrix} . \tag{2.11}$$

As was demonstrated earlier, the polarisation state is fully described with four real parameters, which can be elegantly compressed into two complex ones. Thus the Jones vector **J** utilising two complex amplitudes A_x, A_y can entirely describe the polarisation state of a monochromatic wave and is defined as

$$\mathbf{J} = \begin{bmatrix} E_{0x}e^{i\delta_x} \\ E_{0y}e^{i\delta_y} \end{bmatrix} = \begin{bmatrix} A_x \\ A_y \end{bmatrix} \tag{2.12}$$

The absolute value of intensity is typically unnecessary; therefore, Jones vectors are often normalised to unitary intensity. Furthermore a parameter α is defined by the following relation $\tan\alpha = E_{0y}/E_{0x}$. Since the initial phases are not relevant for the resulting polarisation, we can then rewrite the Jones vector utilising the phase difference $\delta = \delta_y - \delta_x$ in terms of α and δ as

$$\mathbf{J} = \begin{bmatrix} \cos\alpha \\ \sin\alpha\ e^{i\delta} \end{bmatrix} . \tag{2.13}$$

The new parameters α and δ are related with the azimuth θ and the ellipticity angle ϵ through the following relations [13].

$$\tan 2\theta = \tan 2\alpha \cos\delta\ , \tag{2.14}$$

$$\sin 2\epsilon = \sin 2\alpha \sin\delta\ . \tag{2.15}$$

So far, we have been using a Cartesian basis of linear polarisations. Another important basis is the basis of circular polarisations employing the left circular polarisation (LCP) and right circular polarisation (RCP). The process of switching bases is the same as with any other vector transformation and is dictated by the rules of linear algebra along with all other possible operations with Jones vectors. The basis vectors of the mentioned bases are as follows

- The Cartesian basis of linear polarisations:

$$\mathbf{J_x} = \begin{bmatrix} 1 \\ 0 \end{bmatrix} \ , \ \mathbf{J_y} = \begin{bmatrix} 0 \\ 1 \end{bmatrix} \tag{2.16}$$

.

- The circular basis:

$$\mathbf{J_{LCP}} = \frac{1}{\sqrt{2}} \begin{bmatrix} 1 \\ -i \end{bmatrix} \ , \ \mathbf{J_{RCP}} = \frac{1}{\sqrt{2}} \begin{bmatrix} 1 \\ i \end{bmatrix} \tag{2.17}$$

.

Before continuing further, let us introduce the rotation matrix $\mathbf{R}(\varphi)$

$$\mathbf{R}(\varphi) = \begin{bmatrix} \cos\varphi & -\sin\varphi \\ \sin\varphi & \cos\varphi \end{bmatrix} \ . \tag{2.18}$$

This work will utilise it to rotate vectors $\mathbf{v}$ and transform matrices $\mathbf{Q}$ into a rotated basis as follows

$$\mathbf{v}' = \mathbf{R}(\varphi)\mathbf{v} \ , \tag{2.19}$$

$$\mathbf{Q}' = \mathbf{R}\mathbf{Q}\mathbf{R}^{-1} \ , \tag{2.20}$$

where $\mathbf{v}', \mathbf{Q}'$ denote the rotated vector and transformed matrix, respectively.

We will use it to express the Jones vector from equation 2.13 in terms of the polarisation ellipse parameters (θ, ϵ). Let us consider the case of a polarisation ellipse with azimuth equal to zero and ellipticity angle ϵ. Then from 2.14 and 2.15 it follows that $\delta = \pi/2$ and $\alpha = \epsilon$. Substituting these values into 2.13 and then rotating the resulting Jones vector $\mathbf{J}_\epsilon$ by the azimuth θ yields

$$\mathbf{J}_{\theta,\epsilon} = \mathbf{R}(\theta)\mathbf{J}_\epsilon = \begin{bmatrix} \cos\theta & -\sin\theta \\ \sin\theta & \cos\theta \end{bmatrix} \begin{bmatrix} \cos\epsilon \\ i\sin\epsilon \end{bmatrix} = \begin{bmatrix} \cos\epsilon\cos\theta - i\sin\epsilon\sin\theta \\ \cos\epsilon\sin\theta + i\sin\epsilon\cos\theta \end{bmatrix} \ . \tag{2.21}$$

2.2.2 Jones matrix

Jones calculus also enables us to compute the change of polarisation state upon reflection or transmission of fully polarised light through an optical element with the use of Jones matrices.

Suppose an incoming light wave in the coordinate system $\mathbf{S}^{(I)}$ propagates towards an optical element. Upon incidence, part of the wave is reflected. The coordinate system describing the reflected wave shall be denoted $\mathbf{S}^{(R)}$. Another part of the incident wave transmits through the optical element in the coordinate system $\mathbf{S}^{(T)}$. Every coordinate system is aligned so the respective z axes coincide with their respective wavevector as is depicted in 2.2. It is common to use linearly polarised light parallel and perpendicular to the plane of incidence as a basis for Jones vectors. The corresponding polarisations are called p-polarisation and s-polarisation, respectively.

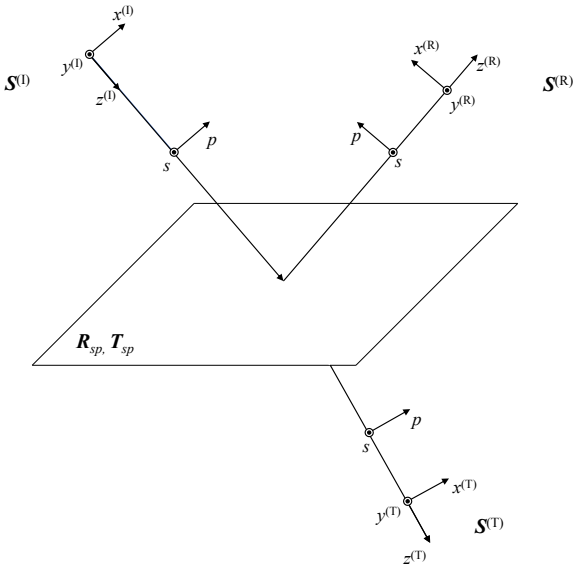

Figure 2.2 Reflection and transmission of light through an optical element with corresponding coordinate systems $\mathbf{S}^{(I)}$ for the incident, $\mathbf{S}^{(R)}$ for the reflected and $\mathbf{S}^{(T)}$ for the transmitted light.

First, let us investigate the reflected light wave. Let us denote the Jones vector of the incident wave $\mathbf{J}^{(I)}$ and the Jones vector of the reflected wave $\mathbf{J}^{(R)}$. We can write the following relationship between them utilising Jones calculus

$$\mathbf{J}^{(R)} = \mathbf{R}_{sp}\mathbf{J}^{(I)} \,, \tag{2.22}$$

where $\mathbf{R}_{sp}$ stands for the *Jones reflection matrix* of the illuminated optical element. This matrix describes changes to the polarisation state of the incident light wave upon reflection off the optical element. By substituting the definition of the Jones vector 2.12 using the aforementioned s, p-polarisation basis into 2.22 and expressing $\mathbf{R}_{sp}$ in terms of its elements we get

$$\begin{bmatrix} A_s^{(R)} \\ A_p^{(R)} \end{bmatrix} = \begin{bmatrix} r_{ss} & r_{sp} \\ r_{ps} & r_{pp} \end{bmatrix} \begin{bmatrix} A_s^{(I)} \\ A_p^{(I)} \end{bmatrix} \,, \tag{2.23}$$

from whence the following relations for the Jones reflection matrix elements are easily derived

$$r_{ss} = \left(\frac{A_s^{(R)}}{A_s^{(I)}} \right)_{A_p^{(I)}=0} , \tag{2.24}$$

$$r_{sp} = \left(\frac{A_s^{(R)}}{A_p^{(I)}} \right)_{A_s^{(I)}=0} , \tag{2.25}$$

$$r_{ps} = \left(\frac{A_p^{(R)}}{A_s^{(I)}} \right)_{A_p^{(I)}=0} , \tag{2.26}$$

$$r_{pp} = \left(\frac{A_p^{(R)}}{A_p^{(I)}} \right)_{A_s^{(I)}=0} . \tag{2.27}$$

In the case of reflection off an optically isotropic sample, the diagonal elements r_{ss}, r_{pp} represent the Fresnel reflection coefficients. The off-diagonal elements represent the mixing of s-polarised and p-polarised light upon reflection and vice versa.

As for the transmitted light wave, we shall follow the same procedure. The change to the polarisation state of the incident light wave upon transmission into the optical element is described by the *Jones transmission matrix* $\mathbf{T}_{sp}$. The Jones vector of transmitted light can be written as

$$\mathbf{J}^{(T)} = \mathbf{T}_{sp}\mathbf{J}^{(I)} . \tag{2.28}$$

Substituting the definition of the Jones vector, with respect to the s, p-polarisation basis, into the above equation 2.28 and writing $\mathbf{T}_{sp}$ in terms of its elements yields

$$\begin{bmatrix} A_s^{(T)} \\ A_p^{(T)} \end{bmatrix} = \begin{bmatrix} t_{ss} & t_{sp} \\ t_{ps} & t_{pp} \end{bmatrix} \begin{bmatrix} A_s^{(I)} \\ A_p^{(I)} \end{bmatrix} , \tag{2.29}$$

which leads to analogous relations for the respective elements of $\mathbf{T}_{sp}$

$$t_{ss} = \left(\frac{A_s^{(T)}}{A_s^{(I)}} \right)_{A_p^{(I)}=0} , \tag{2.30}$$

$$t_{sp} = \left(\frac{A_s^{(T)}}{A_p^{(I)}} \right)_{A_s^{(I)}=0} , \tag{2.31}$$

$$t_{ps} = \left(\frac{A_p^{(T)}}{A_s^{(I)}} \right)_{A_p^{(I)}=0} , \tag{2.32}$$

$$t_{pp} = \left(\frac{A_p^{(T)}}{A_p^{(I)}} \right)_{A_s^{(I)}=0} . \tag{2.33}$$

Here the diagonal elements t_{ss}, t_{pp} stand for the Fresnel transmission coefficients for the case of transmission through an optically isotropic sample.

Once more, the off-diagonal elements hold information about the transformation of one basis linear polarisation into the other upon transmission.

Jones calculus can also be used to describe changes to the polarisation state of light induced by commonly used optical elements. Their Jones matrices are listed below, expressed in the linear (XY) and circular (LR) basis

- Linear polarizer oriented at an arbitrary angle φ with respect to the x axis:

$$\mathbf{P}^{(XY)} = \begin{bmatrix} \cos^2\varphi & \sin\varphi\cos\varphi \\ \sin\varphi\cos\varphi & \sin^2\varphi \end{bmatrix} \ , \ \mathbf{P}^{(LR)} = \begin{bmatrix} 1 & e^{2i\varphi} \\ e^{-2i\varphi} & 1 \end{bmatrix} \tag{2.34}$$

- Phase plate with retardance Γ and fast axis parallel to the x axis:

$$\mathbf{C}^{(XY)} = \begin{bmatrix} 1 & 0 \\ 0 & e^{-i\Gamma} \end{bmatrix} \ , \ \mathbf{C}^{(LR)} = \frac{1}{2}\begin{bmatrix} 1+e^{-i\Gamma} & 1-e^{-i\Gamma} \\ 1-e^{-i\Gamma} & 1+e^{-i\Gamma} \end{bmatrix} \tag{2.35}$$

- Polarisation rotator - rotating the polarisation by an angle ϕ:

$$\mathbf{N}^{(XY)} = \begin{bmatrix} \cos\phi & -\sin\phi \\ \sin\phi & \cos\phi \end{bmatrix} \ , \ \mathbf{N}^{(LR)} = \begin{bmatrix} e^{i\phi} & 0 \\ 0 & e^{-i\phi} \end{bmatrix} \tag{2.36}$$

In order to monitor the polarisation state after the light wave interacts with an optical system consisting of multiple different optical elements, one multiplies the Jones vector of the incident light with the Jones matrices of all present optical elements in the order the light wave encounters them. Suppose a light wave represented with the Jones vector $\mathbf{J}_{\text{IN}}^{(I)}$ propagating through an optical system made up of N optical elements $\mathbf{X}_1$, $\mathbf{X}_2$, …, $\mathbf{X}_N$ indexed in the order the light wave encounters them. Then the resulting Jones vector $\mathbf{J}_{\text{OUT}}^{(I)}$ is

$$\mathbf{J}_{\text{OUT}}^{(I)} = \mathbf{X}_N\mathbf{X}_{N-1}\ldots\mathbf{X}_1\mathbf{J}_{\text{IN}}^{(I)} \ . \tag{2.37}$$

2.3 Complex polarisation parameter

Let us introduce one last parameter used to represent the polarisation state. The previous sections have already demonstrated the description of polarisation states with two parameters (θ, ϵ) or (α, δ). The *complex polarisation parameter* χ is defined as the ratio of the complex amplitudes

$$\chi = \frac{A_y}{A_x} = \tan\alpha e^{i\delta} \ . \tag{2.38}$$

Substituting the complex amplitudes from the Jones vector of a general polarisation state represented in terms of (θ, ϵ) 2.21 into the definition above yields

$$\chi = \frac{\cos\epsilon\sin\theta + i\sin\epsilon\cos\theta}{\cos\epsilon\cos\theta - i\sin\epsilon\sin\theta} = \frac{\tan\theta + i\tan\epsilon}{1 - i\tan\theta\tan\epsilon} \ . \tag{2.39}$$

Assuming small angles θ, ϵ, utilising the approximation $\tan x \approx x$ emerging from the Maclaurin series of the tangent function and assuming the second order term in the denominator to be zero, 2.39 simplifies to

$$\chi \approx \theta + i\epsilon \ . \tag{2.40}$$

2.4 Magneto-optical observables

Magneto-optical (MO) observables are parameters that describe changes in the polarisation state of light waves upon reflection or transmission through a sample inside a magnetic field. The magneto-optical Kerr effect (MOKE) refers to the case of reflection, while the magneto-optical Faraday effect refers to the case of transmission. When light waves interact with isotropic materials via reflection or transmission, there is no transformation of incident s-polarised waves into p-polarised waves or vice versa. This is because the Jones reflection and transmission matrices are diagonal for such materials. However, introducing anisotropy in the material would result in the mixing of the two orthogonal polarisations. In the case of this study, the anisotropy is caused by the magnetic moment of a ferromagnetic material in an external magnetic field.

First, consider the case of an s-polarised wave reflecting off a magnetised ferromagnetic material. The off-diagonal elements of the Jones reflection matrix of such material will no longer be zero. We can use 2.24 and 2.25 to express the ratio of the off-diagonal to diagonal elements of the reflection matrix for an incident s-polarised wave as follows

$$\frac{r_{ps}}{r_{ss}} = \left(\frac{\frac{A_p^{(R)}}{A_s^{(I)}}}{\frac{A_s^{(R)}}{A_s^{(I)}}} \right)_{A_p^{(I)}=0} = \frac{A_p^{(R)}}{A_s^{(R)}}_{A_p^{(I)}=0} = \chi_s^{(R)} \ , \tag{2.41}$$

which can be simplified under the assumption of small angles $\theta_s^{(R)}$, $\epsilon_s^{(R)}$ analogously to 2.39 as

$$\chi_s^{(R)} \approx \theta_s^{(R)} + i\epsilon_s^{(R)} \ . \tag{2.42}$$

We then can define the complex magneto-optical Kerr Angle $\Phi_{K,s}$ for an incident s-polarised wave as

$$\Phi_{K,s} := -\frac{r_{ps}}{r_{ss}} = -\chi_s^{(R)} \ , \tag{2.43}$$

$$\Phi_{K,s} \approx \theta_{K,s}^{(R)} - i\epsilon_{K,s}^{(R)} \ , \tag{2.44}$$

where we have defined two new real parameters Kerr rotation $\theta_{K,s}^{(R)}$ and Kerr ellipticity $\epsilon_{K,s}^{(R)}$. By comparing 2.44 to 2.42 we can deduce the following relations

$$\theta_{K,s}^{(R)} = -\theta_s^{(R)} \ , \tag{2.45}$$

$$\epsilon_{K,s}^{(R)} = \epsilon_s^{(R)} \ . \tag{2.46}$$

Now following an analogous procedure for an incident p-polarised wave with the use of 2.25 and 2.27 we write

$$\frac{r_{sp}}{r_{pp}} = \left(\frac{\frac{A_s^{(R)}}{A_p^{(I)}}}{\frac{A_p^{(R)}}{A_p^{(I)}}} \right)_{A_s^{(I)}=0} = \frac{A_s^{(R)}}{A_p^{(R)}}_{A_s^{(I)}=0} = (\chi_p^{(R)})^{-1} \ . \tag{2.47}$$

To simplify the derivation, we multiply both the numerator and denominator of 2.39 by $\cot\theta$, leaving us with

$$\chi = \frac{1 + i\cot\theta\tan\epsilon}{\cot\theta - i\tan\epsilon} \ . \tag{2.48}$$

This is done so that we may express the cotangent function as a part of a power series. The azimuth of a p-polarised wave is $\pi/2$. Assuming small changes to the azimuth caused upon reflection, $\theta_p^{(R)}$ is close to $\pi/2$ and we can approximate the cotangent function with the first two terms of its Taylor series $\cot\ x_{x\,\approx\,\pi/2} \ \approx\ \pi/2 \ - \ x$. Additionally, again assuming small $\epsilon_p^{(R)}$ and neglecting the imaginary term in the numerator by assuming it close to zero gives

$$\chi_p^{(R)} \approx \frac{1}{\pi/2 - \theta_p^{(R)} - i\epsilon_p^{(R)}} \ , \tag{2.49}$$

$$(\chi_p^{(R)})^{-1} \approx \pi/2 - \theta_p^{(R)} - i\epsilon_p^{(R)} \ . \tag{2.50}$$

The complex magneto-optical Kerr Angle $\Phi_{K,p}$ for an incident p-polarised wave is then analogously defined as

$$\Phi_{K,p} := \frac{r_{sp}}{r_{pp}} = (\chi_p^{(R)})^{-1} \ , \tag{2.51}$$

$$\Phi_{K,p} \approx \theta_{K,p} - i\epsilon_{K,p} \ , \tag{2.52}$$

where we have defined Kerr rotation $\theta_{K,p}$ and Kerr ellipticity $\epsilon_{K,p}$ for an incident incident p-polarised wave similarly to 2.45 and 2.46 as

$$\theta_{K,p} = \pi/2 - \theta_p^{(R)} \ , \tag{2.53}$$

$$\epsilon_{K,p} = \epsilon_p^{(R)} \ . \tag{2.54}$$

The choice of sign in the definitions 2.43 and 2.51 of the Kerr effect for the s and p polarisation, respectively, is not arbitrary. Consider a sample placed in a magnetic field perpendicular to its surface[1] and a light wave propagating at normal incidence along the z axis. The Jones reflection matrix has to respect the symmetry of the system and consequently be invariant to any rotation along the z axis. This requirement can be expressed in a matrix relation using the already defined rotation matrix 2.18 as

$$\mathbf{R}(\varphi)\mathbf{R}_{sp}\mathbf{R}(\varphi) = \mathbf{R}_{sp} \ , \tag{2.55}$$

which yields the following relations for the elements of the Jones reflection matrix

$$r_{sp} = r_{ps} \ , \tag{2.56}$$

$$r_{ss} = -r_{pp} \ . \tag{2.57}$$

Still considering the same example, there is no way to define a plane of incidence and thus no way to define s and p polarisation. Therefore we expect the magneto-optical Kerr effect angles for the s and p polarisation to be equal, which is accomplished by the opposite signs in the aforementioned definitions 2.43 and 2.51.

[1] Defined as polar geometry in section 3.1

Chapter 3

Optically anisotropic media

In the previous chapters, we described light propagation through isotropic media. Anisotropic media were modelled as a black box with a 2x2 reflection and transmission matrix. This chapter aims to describe anisotropy further by first introducing the permittivity tensor and subsequently using it to describe the propagation of light through multi-layer systems with the use of Yeh formalism.

3.1 Permittivity tensor

The permittivity tensor is a material property describing how electric fields interact in a given material. Since light is an electromagnetic wave, parameters measured in this work, such as the MO Kerr angle, depend on the material's permittivity tensor. Knowing the permittivity tensor does allow us to compute the reflection coefficients and, in turn, the MO Kerr angle, but above all, in specific circumstances, we may work backwards and compute the permittivity tensor from a measured MO Kerr angle. In general, the permittivity tensor is a second-order tensor denoted as

$$\boldsymbol{\varepsilon} = \begin{bmatrix} \varepsilon_{xx} & \varepsilon_{xy} & \varepsilon_{xz} \\ \varepsilon_{yx} & \varepsilon_{yy} & \varepsilon_{yz} \\ \varepsilon_{zx} & \varepsilon_{zy} & \varepsilon_{zz} \end{bmatrix} . \tag{3.1}$$

Exposing a ferromagnetic sample to an external magnetic field induces optical anisotropy, which manifests as a small perturbation of the permittivity tensor dependant on the magnetisation of the sample $\mathbf{M}$[1]. The small magnitude of the perturbation allows us to express the perturbed permittivity tensor in the form of a Taylor series centred at zero magnetisation. Seeing as the perturbation is small and the fact that the second-order terms cancel out due to the measuring technique used (see Section 4.4), we will represent the elements of the perturbed permittivity tensor with the first two terms of their Taylor series

$$\varepsilon_{ij}(\mathbf{M}) = \varepsilon_{ij}(0) + \left.\frac{\partial \varepsilon_{ij}}{\partial M_k}\right|_{M_k=0} M_k \ , \tag{3.2}$$

where i, j, k represent any index of the Cartesian basis x, y, z.

[1] Defined as the magnetic dipole moment per unit volume.

Let us define three main geometrical configurations of the magnetisation vector M relative to the sample and the reflected light wave for the description of MOKE. In *polar geometry*, the magnetisation vector is perpendicular to the sample's surface. In *longitudinal geometry*, the magnetisation vector lies within the plane of incidence and the sample's surface. Lastly, in *transverse geometry*, the magnetisation vector is perpendicular to the plane of incidence and lies within the surface of the sample (See Figure 3.1).

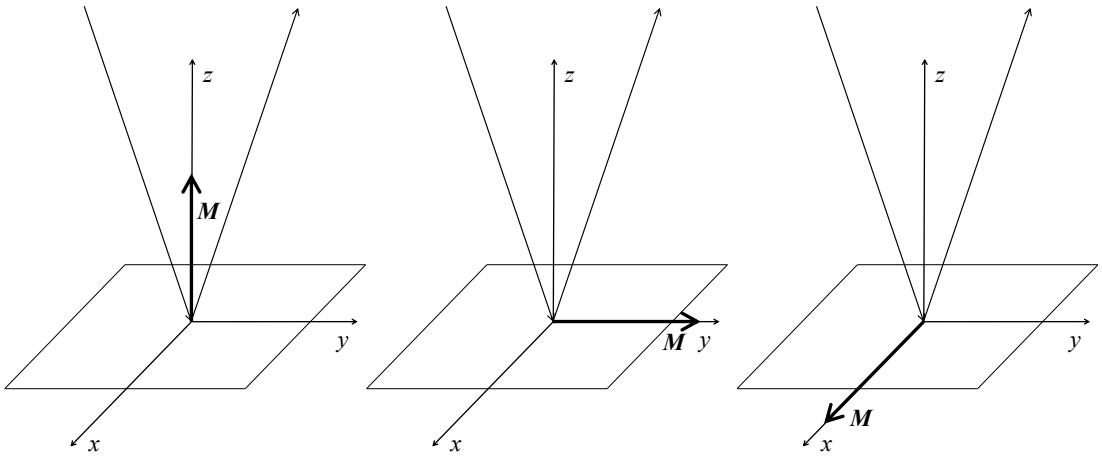

(a) Polar geometry **(b)** Longitudinal geometry **(c)** Transverse geometry

Figure 3.1 Definitions of polar (a), longitudinal (b) and transverse (c) geometries for MOKE measurements of a magnetised sample.

Suppose an optically isotropic ferromagnetic sample is placed into an external magnetic field in polar geometry. The permittivity tensor of such a sample will no longer be diagonal as the external magnetic field magnetised the sample, which introduced optical anisotropy. The new perturbed permittivity tensor has to respect the symmetry of the system according to the Voigt symmetry principle [14]. In polar geometry, the permittivity tensor has to be invariant under any rotation along the z axis, which yields the following general form of the permittivity tensor

$$\boldsymbol{\varepsilon}_p = \begin{bmatrix} \varepsilon_{xx} & \varepsilon_{xy} & 0 \\ -\varepsilon_{xy} & \varepsilon_{xx} & 0 \\ 0 & 0 & \varepsilon_{zz} \end{bmatrix} . \tag{3.3}$$

It can be shown that the restriction to linear magneto-optical effects gives $\varepsilon_{xx} \approx \varepsilon_{zz}$ [15]. This allows us to write the permittivity tensor for polar geometry in a more conventional way as

$$\boldsymbol{\varepsilon}_p = \begin{bmatrix} \varepsilon_1 & i\varepsilon_2 & 0 \\ -i\varepsilon_2 & \varepsilon_1 & 0 \\ 0 & 0 & \varepsilon_1 \end{bmatrix} . \tag{3.4}$$

To obtain the permittivity tensor of the sample in longitudinal geometry, one simply has to rotate the polar coordinate system 90° counterclockwise along the x axis, which results in

$$\boldsymbol{\varepsilon}_l = \begin{bmatrix} \varepsilon_1 & 0 & i\varepsilon_2 \\ 0 & \varepsilon_1 & 0 \\ -i\varepsilon_2 & 0 & \varepsilon_1 \end{bmatrix} . \tag{3.5}$$

The permittivity tensor for the transverse configuration is obtained analogously. Rotating the polar coordinate system clockwise along the y axis results in

$$\boldsymbol{\varepsilon}_t = \begin{bmatrix} \varepsilon_1 & 0 & 0 \\ 0 & \varepsilon_1 & -i\varepsilon_2 \\ 0 & i\varepsilon_2 & \varepsilon_1 \end{bmatrix} . \tag{3.6}$$

3.2 Yeh formalism

Yeh formalism describes the propagation of light through anisotropic layered media. Yeh's original formalism from 1980 [16] was later extended to absorbing materials and MO effects by Professor Višňovský [15]. The formalism allows for calculating the reflected and transmitted wave from an incident wave, assuming the thickness and optical properties of every layer, along with the angle of incidence, are known. By comparing the incident and the calculated reflected wave, we can obtain the reflection matrix elements and hence the MOKE of a multi-layer system, allowing us to model its magneto-optic response.

Let us consider a plane wave impacting an optically anisotropic sample consisting of N distinct layers as depicted in Figure 3.2. Every layer has its corresponding thickness t_k and a permittivity tensor $\boldsymbol{\varepsilon}^{(k)}$. These layers are stacked on top of each other with their surfaces perpendicular to the z axis, meaning the interface between the k^{th} and $(k+1)^{\text{th}}$ layer has coordinates (x, y, z_k), where z_k is constant for every interface. This multi-layer system is surrounded by two semi-infinite half-spaces – 0 and $N+1$ – which are considered optically isotropic and thus are characterised by scalar permittivities $\varepsilon^{(0)}$ and $\varepsilon^{(N+1)}$, respectively. In this work, the substrate shall be considered the $N+1$ half-space as its thickness is orders of magnitude larger than the thickness of all individual layers. The plane of incidence is perpendicular to the x axis, and the angle of incidence is ϕ_0.

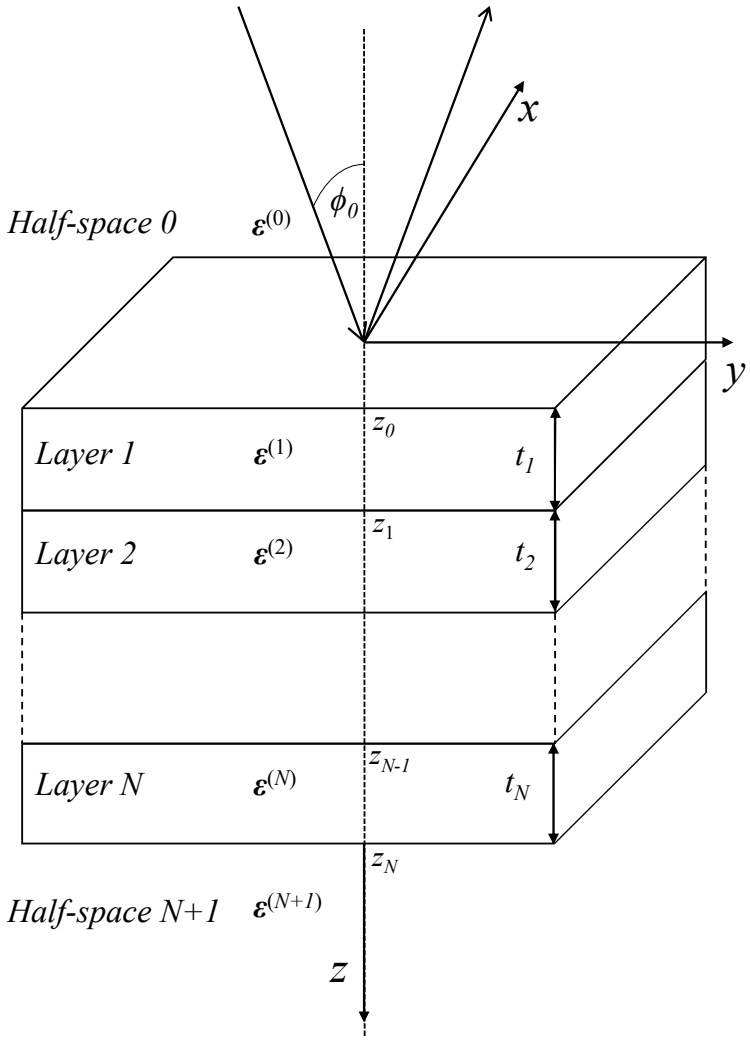

Figure 3.2 Ligthwave impacting a multi-layer sample consisting of N optically anisotropic layers with thicknesses t_k described by the permittivity tensors $\boldsymbol{\varepsilon}^{(k)}$ surrounded by two optically isotropic half-spaces with scalar permittivities $\varepsilon^{(0)}$ and $\varepsilon^{(N+1)}$. The interface between layer k and $k+1$ has coordinates (x, y, z_k).

In order to calculate the reflected wave, we need to solve the wave equation for each layer. Assuming every layer is non-conductive, we can write the wave equation 1.12 for every layer as

$$\Delta \mathbf{E}^{(k)} - \varepsilon_0 \mu_0 \boldsymbol{\varepsilon}^{(k)} \frac{\partial^2 \mathbf{E}^{(k)}}{\partial t^2} - \nabla(\boldsymbol{\nabla} \cdot \mathbf{E}^{(k)}) = 0 \,. \tag{3.7}$$

First, we assume a plane-wave solution

$$\mathbf{E}^{(k)} = \mathbf{E}_0^{(k)} e^{i(\omega t - \mathbf{k}^{(k)} \cdot \mathbf{r})} \,, \tag{3.8}$$

which we substitute into 3.7. Making use of the Einstein summation convention this yields

$$k_j^{(k)} k_j^{(k)} E_{0i}^{(k)} - k_i^{(k)} k_j^{(k)} E_{0j}^{(k)} - \frac{\omega^2}{c^2} \varepsilon_{ij}^{(k)} E_{0j}^{(k)} \,. \tag{3.9}$$

In order to simplify this equation, we introduce the reduced wavevector $\mathbf{N}$ defined as

$$\mathbf{N}^{(k)} = \frac{c}{\omega}\mathbf{k}^{(k)} \ . \tag{3.10}$$

All reduced wavevectors of both reflected and transmitted waves lie in the original plane of incidence; hence the x component of each reduced wavevector is equal to zero. Additionally, from Snell's law, it follows that the N_y component for all layers is equal to

$$N_y = n_0 \sin\varphi_0 \ , \tag{3.11}$$

where n_0 stands for the refractive index of the isotropic half-space 0. Multiplying 3.9 by c^2/ω^2 and substituting in the newly introduced reduced wavevector gives us

$$-N_j^{(k)} N_j^{(k)} E_{0i}^{(k)} + N_i^{(k)} N_j^{(k)} E_{0j}^{(k)} + \varepsilon_{ij}^{(k)} E_{0j}^{(k)} = 0 \ . \tag{3.12}$$

This equation can be rewritten in matrix form as

$$\begin{bmatrix} \varepsilon_{xx}^{(k)} - N_y^2 - (N_z^{(k)})^2 & \varepsilon_{xy}^{(k)} & \varepsilon_{xz}^{(k)} \\ \varepsilon_{yx}^{(k)} & \varepsilon_{yy}^{(k)} - (N_z^{(k)})^2 & \varepsilon_{yz}^{(k)} + N_y N_z^{(k)} \\ \varepsilon_{zx}^{(k)} & \varepsilon_{zy}^{(k)} + N_y N_z^{(k)} & \varepsilon_{zz}^{(k)} - N_y^2 \end{bmatrix} \begin{bmatrix} E_{0x}^{(k)} \\ E_{0y}^{(k)} \\ E_{0z}^{(k)} \end{bmatrix} = 0 \ . \tag{3.13}$$

A non-trivial solution to the equation 3.13 exists only if the determinant of the matrix is equal to zero. Solving the characteristic equation of the matrix

$$\begin{aligned} &(N_z^{(k)})^4 \varepsilon_{zz}^{(k)} + (N_z^{(k)})^3 [N_y(\varepsilon_{yz}^{(k)} + \varepsilon_{zy}^{(k)})] - \\ &- (N_z^{(k)})^2 [\varepsilon_{yy}^{(k)}(\varepsilon_{zz}^{(k)} - N_y^2) + \varepsilon_{zz}^{(k)}(\varepsilon_{xx}^{(k)} - N_y^2) - \varepsilon_{xz}^{(k)}\varepsilon_{zx}^{(k)} - \varepsilon_{yz}^{(k)}\varepsilon_{zy}^{(k)}] - \\ &- N_z^{(k)} N_y [(\varepsilon_{xx}^{(k)} - N_y^2)(\varepsilon_{yz}^{(k)} + \varepsilon_{zy}^{(k)} - \varepsilon_{zx}^{(k)}\varepsilon_{xz}^{(k)} - \varepsilon_{yx}^{(k)}\varepsilon_{xz}^{(k)}] + \\ &+ \varepsilon_{yy}^{(k)} [(\varepsilon_{xx}^{(k)} - N_y^2)(\varepsilon_{zz}^{(k)} - N_y^2)] - \varepsilon_{zx}^{(k)}\varepsilon_{xz}^{(k)}(\varepsilon_{zz}^{(k)} - N_y^2) - \varepsilon_{yz}^{(k)}\varepsilon_{zy}^{(k)}(\varepsilon_{xx}^{(k)} - N_y^2) + \\ &+ \varepsilon_{xy}^{(k)}\varepsilon_{zx}^{(k)}\varepsilon_{yz}^{(k)} + \varepsilon_{yx}^{(k)}\varepsilon_{xz}^{(k)}\varepsilon_{zy}^{(k)} = 0 \ . \end{aligned} \tag{3.14}$$

gives us four roots $N_{zj}^{(k)}$. Each root of 3.14 gives us a solution to 3.13 in the form of

$$\mathbf{e}_j^{(k)} = \begin{bmatrix} -\varepsilon_{xy}^{(k)}(\varepsilon_{zz}^{(k)} - N_y^2) + \varepsilon_{xz}^{(k)}(\varepsilon_{zy}^{(k)} + N_y N_{zj}^{(k)}) \\ (\varepsilon_{zz}^{(k)} - N_y^2)(\varepsilon_{xx}^{(k)} - N_y^2 - (N_{zj}^{(k)})^2) - \varepsilon_{xz}^{(k)}\varepsilon_{zx}^{(k)} \\ -(\varepsilon_{xx}^{(k)} - N_y^2 - (N_{zj}^{(k)})^2)(\varepsilon_{zy}^{(k)} + N_y N_{zj}^{(k)}) + \varepsilon_{xy}^{(k)}\varepsilon_{zx}^{(k)} \end{bmatrix} \ . \tag{3.15}$$

These solutions are known as the proper modes, and they represent polarisation states propagating unchanged through the corresponding medium[2]. We can use these proper modes to form a basis of all possible solutions to 3.13. A general solution to 3.13 can be then written as

$$\mathbf{E}^{(k)} = \sum_{j=1}^{4} E_{0j}^{(k)}(z_k)\mathbf{e}_j^{(k)} e^{i\{\omega t - \frac{\omega}{c}[N_y y + N_{zj}^{(k)}(z - z_k)]\}} \ . \tag{3.16}$$

[2]Proper modes $\mathbf{e}_1^{(k)}$ and $\mathbf{e}_3^{(k)}$ propagate forwards through the multilayer, proper modes $\mathbf{e}_2^{(k)}$ and $\mathbf{e}_4^{(k)}$ represent the reflected wave, hence they propagate backwards.

It can be shown from the Maxwell equations that in electromagnetic plane-waves vectors $\mathbf{N}, \mathbf{E}, \mathbf{B}$ satisfy the following relation

$$\mathbf{B} = \frac{1}{c}\mathbf{N} \times \mathbf{E} \, . \tag{3.17}$$

Using this relation we can obtain the proper magnetic modes $\mathbf{b}_j^{(k)}$ as

$$\mathbf{b}_j^{(k)} = \mathbf{N}_j^{(k)} \times \mathbf{e}_j^{(k)} \, , \tag{3.18}$$

and the magnetic induction vector in terms of its proper modes as

$$\mathbf{B}^{(k)} = \frac{1}{c}\sum_{j=1}^{4} E_{0j}^{(k)}(z_k)\mathbf{b}_j^{(k)} e^{i\{\omega t - \frac{\omega}{c}[N_y y + N_{zj}^{(k)}(z - z_k)]\}} \, . \tag{3.19}$$

After solving the wave equation within each layer of the sample, the next step is implementing the boundary conditions. From Maxwell's equation 1.3, it follows that the tangential components of the electric field vector are continuous at every interface between any two layers. Similarly, from Maxwell's equation 1.1, it follows that the tangential components of the magnetic induction vector are also continuous at the interface between two layers as long as there are no free currents present. In other words for the interface between $(k-1)^{\text{th}}$ and k^{th} layer we can write

$$\sum_{j=1}^{4} E_{0j}^{(k-1)}(z_{k-1})\mathbf{e}_j^{(k-1)} \cdot \mathbf{x} = \sum_{j=1}^{4} E_{0j}^{(k)}(z_k)\mathbf{e}_j^{(k)} \cdot \mathbf{x} e^{i\frac{\omega}{c}N_{zj}^{(k)}t_k} \, , \tag{3.20}$$

$$\sum_{j=1}^{4} E_{0j}^{(k-1)}(z_{k-1})\mathbf{b}_j^{(k-1)} \cdot \mathbf{y} = \sum_{j=1}^{4} E_{0j}^{(k)}(z_k)\mathbf{b}_j^{(k)} \cdot \mathbf{y} e^{i\frac{\omega}{c}N_{zj}^{(k)}t_k} \, , \tag{3.21}$$

$$\sum_{j=1}^{4} E_{0j}^{(k-1)}(z_{k-1})\mathbf{e}_j^{(k-1)} \cdot \mathbf{y} = \sum_{j=1}^{4} E_{0j}^{(k)}(z_k)\mathbf{e}_j^{(k)} \cdot \mathbf{y} e^{i\frac{\omega}{c}N_{zj}^{(k)}t_k} \, , \tag{3.22}$$

$$\sum_{j=1}^{4} E_{0j}^{(k-1)}(z_{k-1})\mathbf{b}_j^{(k-1)} \cdot \mathbf{x} = \sum_{j=1}^{4} E_{0j}^{(k)}(z_k)\mathbf{b}_j^{(k)} \cdot \mathbf{x} e^{i\frac{\omega}{c}N_{zj}^{(k)}t_k} \, , \tag{3.23}$$

which can be again rewritten in matrix form as

$$\mathbf{D}^{(k-1)}\mathbf{E}_0^{(k-1)}(z_{k-1}) = \mathbf{D}^{(k)}\mathbf{P}^{(k)}\mathbf{E}_0^{(k)}(z_k) \, , \tag{3.24}$$

where we have introduced the dynamical matrix $\mathbf{D}^{(k)}$ and the propagation matrix $\mathbf{P}^{(k)}$. The dynamical matrix describes the transformation of the light wave at the interface. Its rows are made up of x and y components of the electric and magnetic proper modes

$$\mathbf{D}^{(k)} = \begin{bmatrix} \mathbf{e}_1^{(k)} \cdot \mathbf{x} & \mathbf{e}_2^{(k)} \cdot \mathbf{x} & \mathbf{e}_3^{(k)} \cdot \mathbf{x} & \mathbf{e}_4^{(k)} \cdot \mathbf{x} \\ \mathbf{b}_1^{(k)} \cdot \mathbf{y} & \mathbf{b}_2^{(k)} \cdot \mathbf{y} & \mathbf{b}_3^{(k)} \cdot \mathbf{y} & \mathbf{b}_4^{(k)} \cdot \mathbf{y} \\ \mathbf{e}_1^{(k)} \cdot \mathbf{y} & \mathbf{e}_2^{(k)} \cdot \mathbf{y} & \mathbf{e}_3^{(k)} \cdot \mathbf{y} & \mathbf{e}_4^{(k)} \cdot \mathbf{y} \\ \mathbf{b}_1^{(k)} \cdot \mathbf{x} & \mathbf{b}_2^{(k)} \cdot \mathbf{x} & \mathbf{b}_3^{(k)} \cdot \mathbf{x} & \mathbf{b}_4^{(k)} \cdot \mathbf{x} \end{bmatrix} \, . \tag{3.25}$$

The propagation matrix $\mathbf{P}^{(k)}$ describes the propagation of light through the k^{th} layer

$$\mathbf{P}^{(k)} = \begin{bmatrix} e^{i\frac{\omega}{c}N_{z1}^{(k)}t_k} & 0 & 0 & 0 \\ 0 & e^{i\frac{\omega}{c}N_{z2}^{(k)}t_k} & 0 & 0 \\ 0 & 0 & e^{i\frac{\omega}{c}N_{z3}^{(k)}t_k} & 0 \\ 0 & 0 & 0 & e^{i\frac{\omega}{c}N_{z4}^{(k)}t_k} \end{bmatrix} . \tag{3.26}$$

Multiplying 3.24 from the left by the inverse of the dynamical matrix for the $(k-1)^{\text{th}}$ layer gives us a relation between amplitudes of all the proper modes in two adjacent layers in the form of the transfer matrix $\mathbf{T}^{(k-1,k)}$

$$\mathbf{E}_0^{(k-1)} = (\mathbf{D}^{(k-1)})^{-1}\mathbf{D}^{(k)}\mathbf{P}^{(k)}\mathbf{E}_0^{(k)} = \mathbf{T}^{(k-1,k)}\mathbf{E}_0^{(k)} . \tag{3.27}$$

The transfer matrix can be constructed for all interfaces except the last one. We consider the substrate semi-infinite, meaning there is no way to construct its propagation matrix. The transfer matrix $\mathbf{T}^{(N,N+1)}$ is then defined as

$$\mathbf{E}_0^{(N)} = (\mathbf{D}^{(N-1)})^{-1}\mathbf{D}^{(N+1)}\mathbf{E}_0^{(N+1)} = \mathbf{T}^{(N,N+1)}\mathbf{E}_0^{(N+1)} . \tag{3.28}$$

Applying this procedure for each interface, we can construct the matrix M characterising the entire anisotropic multi-layer system as

$$\mathbf{E}_0^{(0)} = \left(\prod_{k=1}^{N+1}\mathbf{T}^{(k-1,k)}\right)\mathbf{E}_0^{(N+1)} = \mathbf{M}\mathbf{E}_0^{(N+1)} . \tag{3.29}$$

Now suppose a polarised light wave is interacting with an arbitrary multi-layer system characterised by the matrix M. The choice of proper modes in the optically isotropic half-space 0 is arbitrary. The incident wave can be decomposed into two orthogonal, but not necessarily linear, proper modes $\mathbf{e}_1^{(0)}$ and $\mathbf{e}_3^{(0)}$ with their respective amplitudes $E_{01}^{(0)}$ and $E_{03}^{(0)}$. Let us assume these proper modes to be the s and p polarisations for the following derivation. Let us assume the same for the proper modes of the reflected wave $\mathbf{e}_2^{(0)}$ and $\mathbf{e}_4^{(0)}$ with amplitudes $E_{02}^{(0)}$ and $E_{04}^{(0)}$. We assume the same orthogonal basis of proper modes for the incident and reflected wave except for the z-component pointing in the opposite direction. If we define proper modes of the optically isotropic substrate analogously, we get $E_{02}^{(N+1)}$, $E_{04}^{(N+1)}$ = 0, since there is no reflected wave propagating through the substrate. Substituting all of this into 3.29 and expressing the matrix M in terms of its elements yields

$$\begin{bmatrix} E_{01}^{(0)} \\ E_{02}^{(0)} \\ E_{03}^{(0)} \\ E_{04}^{(0)} \end{bmatrix} = \begin{bmatrix} M_{11} & M_{12} & M_{13} & M_{14} \\ M_{21} & M_{22} & M_{23} & M_{24} \\ M_{31} & M_{32} & M_{33} & M_{34} \\ M_{41} & M_{42} & M_{43} & M_{44} \end{bmatrix} \begin{bmatrix} E_{01}^{(N+1)} \\ 0 \\ E_{03}^{(N+1)} \\ 0 \end{bmatrix} . \tag{3.30}$$

We can now express all the reflection coefficients according to their definitions 2.24-2.27 in terms of elements of the matrix M as

$$r_{ss} = \left(\frac{E_{02}^{(0)}}{E_{01}^{(0)}} \right)_{E_{03}^{(0)}=0} = \frac{M_{21}M_{33} - M_{23}M_{31}}{M_{11}M_{33} - M_{13}M_{31}} \,, \tag{3.31}$$

$$r_{sp} = \left(\frac{E_{02}^{(0)}}{E_{03}^{(0)}} \right)_{E_{01}^{(0)}=0} = \frac{M_{11}M_{23} - M_{21}M_{13}}{M_{11}M_{33} - M_{13}M_{31}} \,, \tag{3.32}$$

$$r_{ps} = -\left(\frac{E_{04}^{(0)}}{E_{01}^{(0)}} \right)_{E_{03}^{(0)}=0} = -\frac{M_{41}M_{33} - M_{43}M_{31}}{M_{11}M_{33} - M_{13}M_{31}} \,, \tag{3.33}$$

$$r_{pp} = -\left(\frac{E_{04}^{(0)}}{E_{03}^{(0)}} \right)_{E_{01}^{(0)}=0} = -\frac{M_{11}M_{43} - M_{41}M_{13}}{M_{11}M_{33} - M_{13}M_{31}} \,. \tag{3.34}$$

The negative sign in front of the reflection coefficients r_{ps} and r_{pp} stems from the proper modes chosen in the last paragraph. Contrary to 2.2, the reflected p-polarisation does not change orientation which is compensated for by the added minus sign.

With the calculated reflection coefficients, we have everything needed to calculate the MO response of any arbitrary multi-layer system. Furthermore, we may use this process in reverse and numerically determine the off-diagonal permittivity tensor elements from the knowledge of the MO Kerr effect and the diagonal elements for any of the geometries defined in Figure 3.1.

Chapter 4

Experimental techniques

This chapter introduces the experimental methods utilised to prepare and subsequently analyse the samples studied in this work. First, pulsed laser deposition (PLD) will be introduced as a means to grow thin layers. Afterwards, we will present atomic force microscopy used for the analysis of sample surfaces. Lastly, two more experimental techniques – spectroscopic ellipsometry and magneto-optical spectroscopy – will be introduced, and their workings will be explained in terms of the Jones calculus.

4.1 Pulsed laser deposition

Pulsed laser deposition is a physical vapour deposition technique popularised in the late 1980s as a fast and reproducible way to grow thin oxide films. Its main virtues are the ability to grow good quality epitaxial thin oxide films and stoichiometric transfer between the target and the substrate [17]. These, among others, make PLD an excellent choice for growing epitaxial films of multicomponent inorganic materials, such as LSMO.

Figure 4.1 depicts a typical PLD set-up. A dense target made from the material we wish to deposit is placed inside a vacuum chamber. A system of lenses focuses short ($\sim$ ns) high energy density ($\sim$ J/cm^2) laser pulses onto the target. Each pulse ablates a small part of the target creating a plasma plume. The plasma plume is launched upwards, carrying the ablated material onto the substrate providing material flux for film growth.

In order to achieve epitaxial growth, the plume must consist of atomic, diatomic, or other low-mass components. This is accomplished by choosing an ultraviolet wavelength laser and a short pulse width.[1] Such pulses are strongly absorbed by a small volume of the target [17].

PLD is often done with the presence of a background gas. The background gas serves two purposes. First, the formation of some thin-film materials requires a reactive species (oxides require molecular oxygen). The background gas also serves as a protective buffer for the growing layer. Kinetic energies of the plume can reach up to several hundred eV, enough to damage the growing film. A background gas can reduce plume energies to much less than 1 eV [17].

[1] In this work, a KrF laser emitting light at 248 nm was selected.

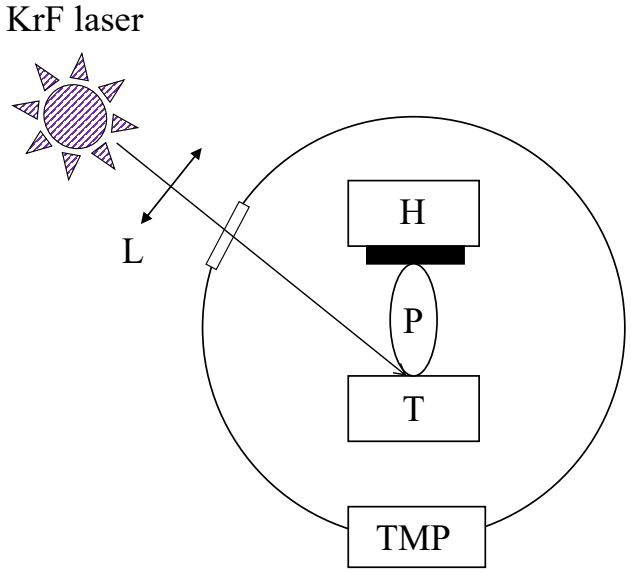

Figure 4.1 Schematic diagram of a PLD set-up. Pulses from the ultraviolet KrF laser are focused by a system of lenses (L) into a vacuum chamber with a turbo-molecular pump (TMP). The pulses impact a solid target (T), creating a plasma plume (P). The plume carries the ablated material towards the substrate attached to a heater (H).

A post-deposition oxygen annealing is known to improve the quality of fabricated thin oxide films by oxidising the film or, conversely, by removing excess oxygen. This treatment leads to significant improvements in Curie temperature and CMR [18].

4.2 Atomic force microscopy

Atomic force microscopy (AFM) is a surface imaging technique regarded for its very high spatial resolution (up to 0.1 nm for vertical resolution and 1 nm for lateral resolution [19]).

A schematic diagram of a typical AFM set-up can be seen in Figure 4.2. A very sharp tip ($\sim$ nm) is attached to a flexible cantilever. The analysed sample is moved by a set of piezoelectric actuators, making the AFM tip scan along the sample's surface. As the tip is scanning the surface, the cantilever mechanically bends as a result of the Van der Waals and electrostatic forces acting on the tip. This movement is then tracked by a laser and a photodetector. A topographical image of the sample's surface is then obtained by relating the recorded movement of the cantilever to the magnitude of short-range forces exerted on the tip.

The most basic mode of AFM operation is the static contact mode. In static contact mode, the tip is dragged along the surface, and the image is constructed directly from the cantilever's deflection. Although this approach is simple, it is burdened by practical difficulties. In ambient conditions, the tip is usually attracted to the sample's surface due to capillary condensation, making the tip stick to the sample.

As the tip scans the surface, the sample experiences both compressive stress from the tip-sample interaction and shear stress related to the lateral scanning movement. This can induce deformation in the analysed sample, or worsen image quality by degrading the tip.

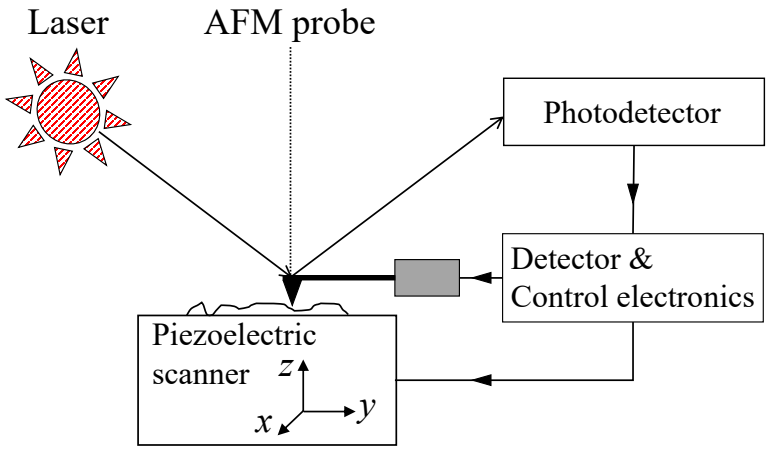

Figure 4.2 Schematic diagram of an AFM set-up. Piezoelectric scanners move with the sample. As the sample moves, the AFM probe tip is affected by short-range forces. The resulting movement of the tip is tracked by a laser and a photodetector, which feeds recorded data to the detector and the control electronics.

To combat these difficulties, *tapping mode* AFM is utilised. In tapping mode, the tip oscillates near its resonant frequency with a constant amplitude. The tip is made to strike the surface during each oscillation. The oscillation energy is set so that the tip overcomes the stickiness of the surface. The image is then produced from the changes in oscillation amplitude caused by the differences in surface height. This eliminates the shear stress while also subjecting the sample to lower compressive stress [19].

4.3 Spectroscopic ellipsometry

Spectroscopic ellipsometry (SE) is an experimental technique used to analyse the optical response of a material.

A schematic diagram of a rotating compensator ellipsometry set-up (RCE) is depicted in Figure 4.3. First, the light from a wide-spectrum lamp passes through the polariser P. The polarised light then reflects off sample S before passing through a rotating compensator C, analyser A and ultimately into a detector D.

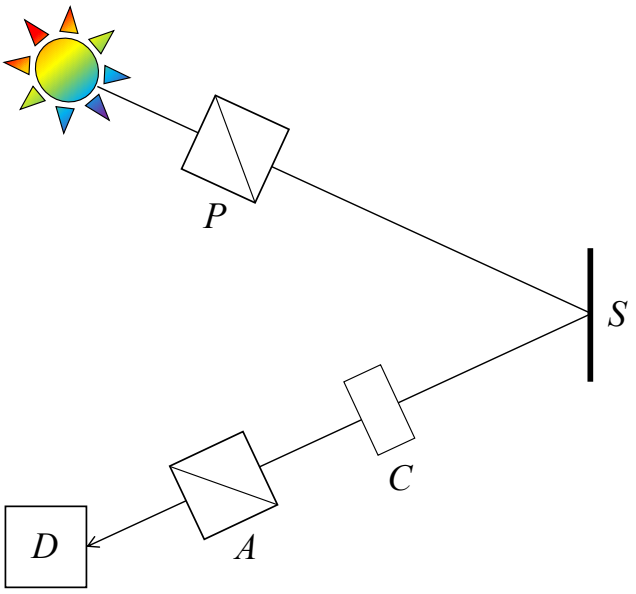

Figure 4.3 Schematic of the rotating compensator ellipsometry set-up. Light from a wide-spectrum lamp passes through polariser P, reflects off sample S, continuing through a rotating compensator C, analyser A and into a detector D.

Next, we will make use of Jones formalism to calculate the resulting polarisation state of the detected light. We will be working in the basis of s and p polarisations as defined in Figure 2.2.

The light from the wide-spectrum lamp is polarised by a polariser P oriented at an angle ξ measured from the x axis. The Jones transmission matrix $\mathbf{P}$ of the polariser is given by 2.34

$$\mathbf{P} = \begin{bmatrix} \cos^2 \xi & \sin \xi \cos \xi \\ \sin \xi \cos \xi & \sin^2 \xi \end{bmatrix} . \tag{4.1}$$

Reflection off the sample is characterised by the Jones reflection matrix as defined in 2.22. Assuming the sample is optically isotropic, we can write its Jones reflection matrix $\mathbf{R}$ in a simplified diagonal form as

$$\mathbf{R}_{sp} = \begin{bmatrix} r_{ss} & 0 \\ 0 & r_{pp} \end{bmatrix} . \tag{4.2}$$

The rotating compensator C is a phase plate with retardance Γ and a fast axis rotated at an angle φ from the x axis. The Jones transmission matrix of an unrotated compensator is given by 2.35. We get the Jones transmission matrix of the rotated compensator by rotating the coordinate system with the use of 2.18 as

$$\mathbf{R}(\varphi)\mathbf{C}\mathbf{R}(-\varphi) = \begin{bmatrix} \cos \varphi & -\sin \varphi \\ \sin \varphi & \cos \varphi \end{bmatrix} \begin{bmatrix} 1 & 0 \\ 0 & e^{-i\Gamma} \end{bmatrix} \begin{bmatrix} \cos \varphi & \sin \varphi \\ -\sin \varphi & \cos \varphi \end{bmatrix} . \tag{4.3}$$

The analyser A is a linear polariser oriented at an angle ζ measured from the x axis and its Jones transmission matrix is given analogously to 4.1 by

$$\mathbf{A} = \begin{bmatrix} \cos^2 \zeta & \sin \zeta \cos \zeta \\ \sin \zeta \cos \zeta & \sin^2 \zeta \end{bmatrix} . \tag{4.4}$$

Finally, we can write the Jones vector of the detected light $\mathbf{J}_{\mathrm{OUT}}$ in agreement with 2.37 as

$$\mathbf{J}_{\mathrm{OUT}} = \mathbf{A}\mathbf{R}(\varphi)\mathbf{C}\mathbf{R}(-\varphi)\mathbf{R}_{sp}\mathbf{P}\mathbf{J}_{\mathrm{IN}} \ , \tag{4.5}$$

from which we can determine the detected intensity as

$$I = (\mathbf{J}_{\mathrm{OUT}})^{+}(\mathbf{J}_{\mathrm{OUT}}) \ . \tag{4.6}$$

Spectroscopic ellipsometry measures the change between the s and p components of the incident wave upon reflection off the sample. This change is expressed in terms of the complex reflectance ratio ρ defined as the ratio of the r_{pp} and r_{ss} elements of the sample's reflection matrix

$$\rho = \frac{r_{pp}}{r_{ss}} = \tan(\Psi)e^{i\Delta} \ , \tag{4.7}$$

where we have also introduced the ellipsometric angles Ψ and Δ. These can be extracted from the intensity calculated according to 4.5 and 4.6. The calculation will not be presented in this work as it is quite complex and can be found in [20]. Spectral measurement of the ellipsometric angles allows us to calculate the optical properties of the sample, namely the refraction index n and extinction coefficient k. These two parameters are often combined into the complex refraction index $\tilde{n} = n + ik$, which is related to the diagonal element of the permittivity tensor ε_1 as

$$\varepsilon_1 = (\tilde{n})^2 \ . \tag{4.8}$$

In this work, we are analysing intricate multilayer samples. In order to calculate the complex refraction index of a layer in such a sample, multiple reflections inside the sample need to be considered. For that reason, the computation of the complex refraction index is done numerically by software, typically with full knowledge of all optical and physical parameters of layers other than the layer of interest.

4.4 Magneto-optical spectroscopy

MO spectroscopy is a suite of highly sensitive experimental techniques capable of measuring the, usually small, MO Kerr angles θ_K and ε_K. MO spectroscopy can be further divided based on the quantity measured. In this work we employ rotating analyser MO spectroscopy, which falls into the intensity based class of MO spectroscopy measurements. It was shown that this technique can achieve similar or even higher signal to noise ratio as the other ellipticity or azimuth modulation based methods [21]. Its precision makes it suitable to measure MO signals from thin-layers, which allows us to calculate their off-diagonal permittivity tensor elements as discussed in Section 3.2.

MO spectroscopy is fundamentally similar to SE discussed above. The main difference is the ferromagnetic sample's exposure to a magnetic field during measurement, inducing optical anisotropy in the sample. The actual measurement set-up differs from SE in the rotating element. We will be using a static compensator and a rotating analyser.[2] A schematic diagram of this set-up can be found below in Figure 4.4.

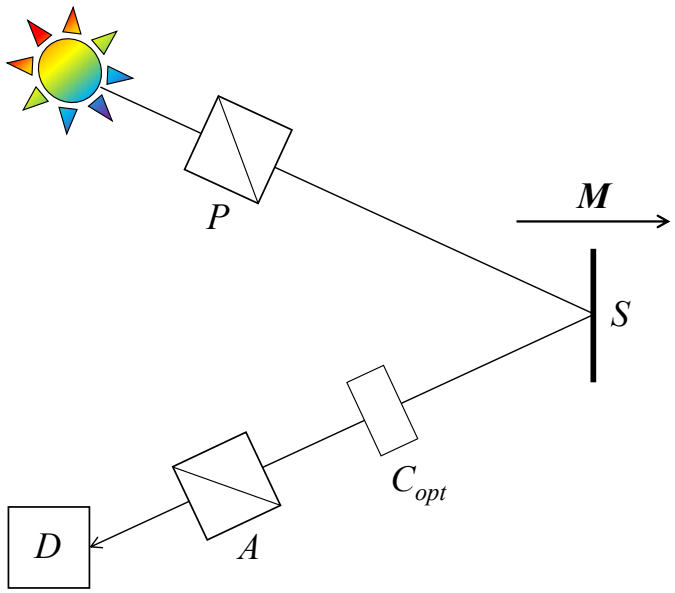

Figure 4.4 Light from a wide-spectrum lamp passes through polariser P, reflects off sample S with induced magnetisation $\mathbf{M}$ and continues onward passing through an optional compensator C_{opt}, analyser A and ultimately into a detector D.

Regarding the MO spectroscopy set-up itself, first light from a wide-spectrum lamp passes through a polariser P before reflecting off the sample S placed inside a magnetic field. The reflected beam then continues through an optional compensator C_{opt}, a rotating analyser A and finally into the detector D.

Analogously to SE, we will use Jones calculus and the s, p basis of linear polarisations to calculate the detected light intensity. For the polariser P oriented at an angle ξ, we will use 4.1. Transmission through the compensator with retardance Γ will be described by 2.35. The analyser oriented at an arbitrary angle ζ will be described by 4.4.

The Jones reflection matrix of the sample will no longer be diagonal due to the anisotropy induced by the magnetic field and thus will have the general form as written in 2.22. Assuming the sample to be magnetised in polar geometry and the angle of incidence to be approximately zero, we can use identities 2.56, 2.57 and the definition of the MO Kerr angle 2.43 to rewrite the Jones reflection matrix of the sample as

$$\mathbf{R}_{sp} = \begin{bmatrix} 1 & -\Phi_K \\ -\Phi_K & -1 \end{bmatrix} . \tag{4.9}$$

[2] This set-up can also be used for SE and is commonly referred to as RAE.

In agreement with 2.37 we can write the Jones vector of the detected light as

$$\mathbf{J}_{\text{OUT}} = \mathbf{ACR}_{sp}\mathbf{PJ}_{\text{IN}} \, . \tag{4.10}$$

Let us now consider the specific case of the set-up used to analyse the samples. The polariser P is set at 90°, and thus the light reflecting off the samples is p-polarised. The angle ζ of the analyser A is measured from the crossed position. Applying the above to 4.10 yields

$$\mathbf{J}_{\text{OUT}} = \begin{bmatrix} \cos^2\zeta & \sin\zeta\cos\zeta \\ \sin\zeta\cos\zeta & \sin^2\zeta \end{bmatrix} \begin{bmatrix} 1 & 0 \\ 0 & e^{-i\Gamma} \end{bmatrix} \begin{bmatrix} 1 & -\Phi_K \\ -\Phi_K & -1 \end{bmatrix} \begin{bmatrix} 0 \\ 1 \end{bmatrix} \, . \tag{4.11}$$

Multiplying all the Jones matrices with the Jones vector of the incident light, we arrive at the Jones vector of detected light

$$\mathbf{J}_{\text{OUT}} = \begin{bmatrix} -\Phi_K\cos^2\zeta - e^{-i\Gamma}\sin\zeta\cos\zeta \\ -\Phi_K\sin\zeta\cos\zeta - e^{-i\Gamma}\sin^2\zeta \end{bmatrix} \, , \tag{4.12}$$

from which the light's intensity can be calculated according to 4.6. Substituting 4.12 into 4.6 gives us the intensity of detected light as

$$I = \sin^2\zeta + |\Phi_K|^2\cos^2\zeta + \sin(2\zeta)\mathrm{Re}\Big\{\Phi_K e^{i\Gamma}\Big\} \, . \tag{4.13}$$

The quadratic term in Φ_K can be neglected as the magnitude of the Kerr effect of thin layers is very small. The absolute value of intensity was neglected throughout the calculation; hence the left side of the equation should be multiplied by a multiplier I_0. We should also account for dark current inside the detector, which is done by introducing an additive constant I_{dark}. Following through on the above we can rewrite 4.13 in terms of the Kerr rotation θ_K and Kerr ellipticity ε_K as

$$I = I_0[\sin^2\zeta + |\Phi_K|^2\cos^2\zeta + \sin(2\zeta)(\theta_K\cos\Gamma + \varepsilon_K\sin\Gamma)] + I_{\text{dark}} \, . \tag{4.14}$$

The above equation enables us to calculate both the Kerr rotation and Kerr ellipticity by conducting the following sequence of measurements. First, the intensity is measured for a number of analyser angles ζ without a phase plate, or in other words, with $\Gamma = 0$. Then from 4.14, we can fit the measured intensity as a function of ζ with θ_K being a constant parameter for each wavelength. The second measurement is done with the phase-plate present. One could follow the same procedure for the Kerr ellipticity if Γ were $\pi/2$, but, unfortunately, no phase plate can deliver constant retardance throughout a broad spectrum. The second measurement then measures the effect of both θ_K and ε_K. Assuming the spectral dependence of Γ is known, the intensity from the second measurement can be fitted as a function of ζ with $(\theta_K\cos\Gamma + \varepsilon_K\sin\Gamma)$ being the constant parameter for each wavelength. Since θ_K is already known, ε_K can be extracted from the result of the fit.

The sensitivity of the measurements described above is further improved by doing each measurement twice, once with each possible orientation of the magnetic field in polar geometry. Taking the difference of the Kerr angles from the two measurements with the opposite orientations of the magnetic field gives us two times the Kerr angle while eliminating both any unwanted optical effects and the quadratic MO Kerr effect.

Chapter 5

Structural and magnetic properties of $La_{2/3}Sr_{1/3}MnO_3$

The following chapter includes a brief overview of the physical properties of $La_{2/3}Sr_{1/3}MnO_3$ (LSMO). Firstly, the material structure of bulk LSMO will be introduced. Secondly, a short review of ferromagnetism is included before we present the magnetic properties of bulk LSMO.

5.1 Structure of bulk LSMO

LSMO is a hole-doped manganese oxide. Its ideal crystallographic structure is the cubic perovskite. The perovskite structure is shown for an arbitrary ABO_3 oxide in Figure 5.1. A-site atoms form a cubic cell. A BO_6 octahedron is nested inside this cube, with the oxygen atoms lying in the centre of the faces of the cube. The B-site atom lies in the centre of the octahedron.

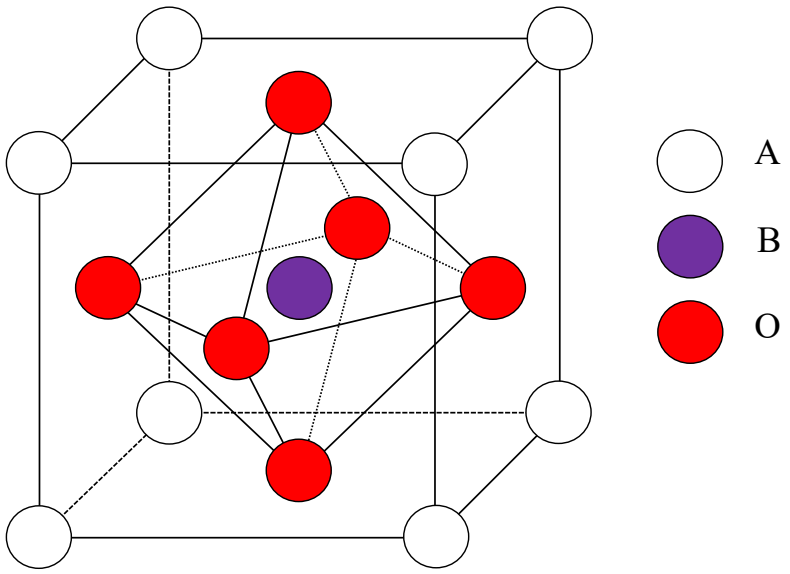

Figure 5.1 A schematic depiction of the ideal cubic perovskite structure ABO_3. A BO_6 octahedron centred at the B-site is nested inside the cube.

The structure of manganese oxides is dictated by the tolerance factor t, which is defined as

$$t := \frac{r_A + r_O}{\sqrt{2(r_B + r_O)}} , \tag{5.1}$$

where r_A, r_B and r_O represent the ionic radii of the A and B atoms and oxygen, respectively. For an ideal cubic perovskite structure $t = 1$. The structure remains stable for 0.89 < t < 1.02 [22]. Generally, t greatly differs from 1 due to varying cation radii leading to rhombohedral or orthorhombic structure. When $LaMnO_3$ is doped by Sr, it becomes rhombohedral LSMO with lattice parameters $a = 5.47$ Å and α = 60.43° [23].

5.2 Ferromagnetism

Ferromagnetism is one of the four basic types of magnetic ordering. It is characterised by the formation of *magnetic domains*; regions where spins of unpaired electrons align in parallel. Naturally these domains are not uniformly aligned throughout the material, yielding zero net magnetisation. However, these domains can be aligned in the same direction by applying an external magnetic field to the material. The resulting magnetisation as a function of the magnitude of the external magnetic field traces a *hysteresis loop*, which can be seen in Figure 5.2. This loop is commonly described using three parameters. The saturation magnetisation M_s is the maximum achievable magnetisation of the sample. The remanent magnetisation M_r measures the remaining magnetisation after the external magnetic field has been set to zero. Lastly, the coercivity H_c describes the magnetic field required to set the magnetisation back to zero.

The saturation magnetisation M_s is an intrinsic property inherent to the material itself. On the other hand, the remanent magnetisation M_r and coercivity H_c are extrinsic and thus are dependent on many external factors, among which are the geometry of the sample, microscopic defects, thermal history and the rate of change of the magnetic field [24].

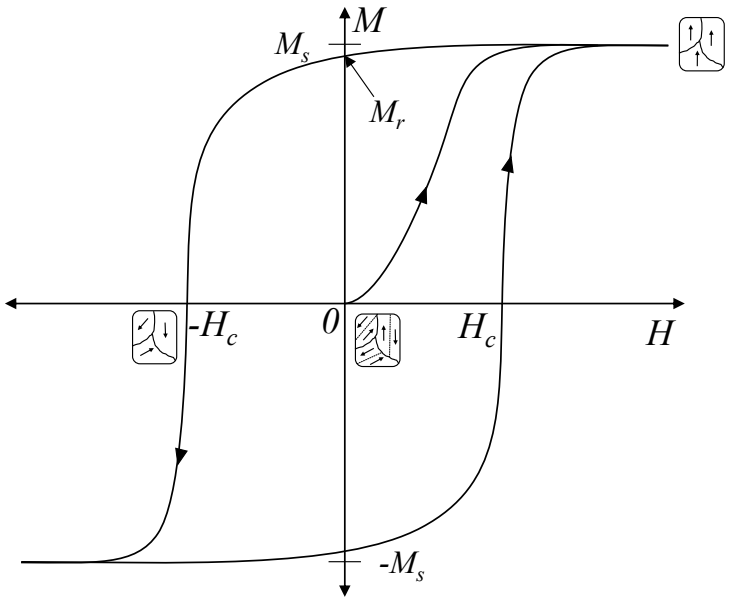

Figure 5.2 The hysteresis loop of a ferromagnetic material. At zero external field in an unmagnetised virgin state. An increasing magnetic field magnetises the material until all magnetic moments across domains are aligned and saturation magnetisation M_s is reached. After setting the magnetic field back to zero, remanent magnetisation M_r remains. A magnetic field of magnitude H_c is required for zero net magnetisation.

5.3 Magnetic properties of LSMO

The magnetic ordering in LSMO has been explained by C. Zener [6]. He found that the origin of LSMO's ferromagnetic ordering lies in the double-exchange (DE) interaction between manganese ions of mixed valence enabled by the overlap of manganese d-orbitals and oxygen p-orbitals.

In ambient conditions, pure $LaMnO_3$ is neither ferromagnetic [2] nor is it a good conductor [25]. In this stoichiometry, each manganese atom must be triply charged resulting in the ionic composition $La^{3+}Mn^{3+}O_3^{2-}$. The manganese ions in Mn^{3+}–O^{2-}–Mn^{3+} bonds present in this compound can undergo both ferromagnetic and antiferromagnetic ordering, but only at very low temperatures [26].

Substituting some of the lanthanum atoms with strontium leads to a corresponding number of Mn^{3+} becoming quadruply charged Mn^{4+} since strontium has a maximum valence of 2+. The presence of mixed Mn^{3+}/Mn^{4+} ions leads to ferromagnetic ordering through the *double exchange* interaction which is schematically depicted in Figure 5.3. In this interaction, an e_g electron transfer occurs from the Mn^{3+} ion to the O^{2-} ion simultaneously with a transfer of an electron from the O^{2-} ion to the Mn^{4+} ion. The minimal energy of the system is achieved when the spins in the Mn^{3+}–O^{2-}–Mn^{4+} and the Mn^{4+}–O^{2-}–Mn^{3+} state point in the same direction, which leads to ferromagnetic ordering [6].

LSMO is a half-metal meaning it is a conductor for electrons with one orientation of spin while being an insulator for electrons with the other orientation. This behaviour and the conductivity of LSMO, in general, are also explained by the DE interaction.

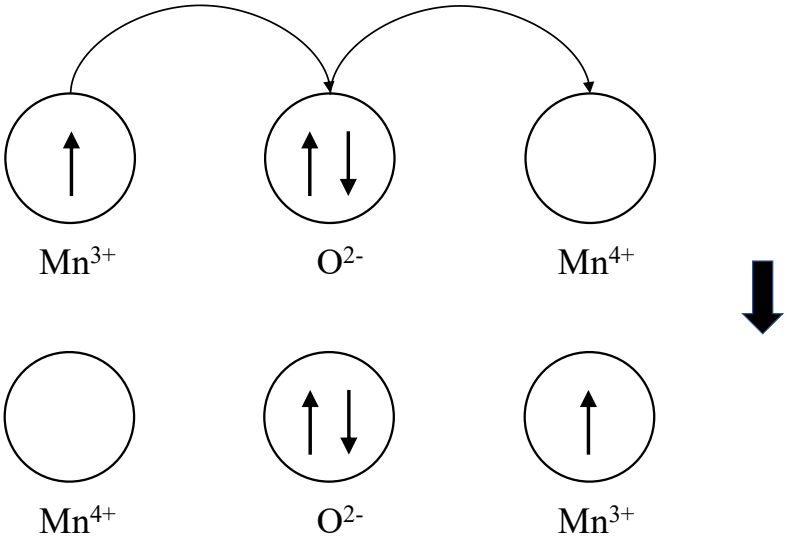

Figure 5.3 Schematic diagram of the double exchange interaction between d-shells of Mn^{3+} and Mn^{4+} ions via the $2p$ state of O^{2-}.

The presence of Sr atoms also affects the Curie temperature (i.e. the temperature below which ferromagnetic ordering takes place). The stoichiometry $La_{2/3}Sr_{1/3}MnO_3$ chosen for this work possesses the highest curie temperature of $T_C \sim 370$ K [2] while also exhibiting good conductivity [25].

Chapter 6

Investigated samples

This chapter will familiarise the reader with the investigated samples. It will give insight into the structure and properties of LSMO thin films deposited onto silicon with an intermediary nanosheet buffer layer.

6.1 Thin film LSMO

Depositing a material as a thin film results in modifications in its crystallographic structure. These changes are induced by epitaxial strain caused by a difference in lattice parameters between the substrate and the material of the thin film. Denoting a_l and a_s as the bulk in-plane lattice parameters of the deposited material and the substrate, respectively, *lattice mismatch* m can be defined as

$$m := \frac{a_l - a_s}{a_s} \,. \tag{6.1}$$

Negative values of m correspond to a thin film grown under tensile strain, while positive values of m to a film grown under compressive strain.

One of the effects caused by epitaxial strain in LSMO is the change in the ordering of the manganese atom $3d$ electron energy levels. For a manganese atom in a spherically symmetric field, all five $3d$ energy levels are degenerated. These five levels split into two, e_g and t_{2g}, under the effect of a crystal field with perfect cubic symmetry. Epitaxial strain further lowers the symmetry, which in turn causes further lifting of the degeneracy. The ferromagnetic double-exchange interaction is mainly exhibited in structures with strongly degenerated e_g energy levels; hence epitaxial strain has been tied to suppression of the double-exchange mechanism [21]. The formation of a magnetically inert layer at the LSMO/substrate interface was also attributed to the suppression of the double exchange caused by epitaxial strain [27].

Magnetic anisotropy of LSMO is also greatly affected by epitaxial strain. For bulk LSMO, the easy axis of magnetisation lies in the pseudocubic [111] direction [28]. Epitaxial strain typically shifts this axis into the plane of the film. The orientation of easy axes of magnetisation exhibit strong dependence on the type of epitaxial strain and temperature [29].

6.2 $Ca_2Nb_3O_{10}$ nanosheets

Growing high-quality textured LSMO thin films on low-cost substrates such as silicon would prove beneficial for future large-scale industrial adaptation. However, growing LSMO directly on silicon results in low crystalline quality of the film [30] along with a major degradation of LSMO's properties. This is due to substantial differences in their respective crystalline structure and their reactivity with oxygen [8]. In order to deposit LSMO with a higher crystiline quality on silicon we introduce a nanosheet (NS) seed layer onto the substrate to facilitate textured growth. In this study, $Ca_2Nb_3O_{10}$ (CNO) nanosheets were used.

CNO nanosheets are made by exfoliating $KCa_2Nb_3O_{10}$ (KCNO) prepared by a solid-state route from precursor oxides. KCNO crystallises in a monoclinic structure but is usually described using a larger tetragonal unit cell. Its structure comprises a repeating motif of three perovskite layers laying in the (001) plane and a K^+ cation layer [31]. Exfoliating KCNO creates a two-dimensional lattice of nanosheets with a square a-b plane. This lattice has a lattice parameter a_{NS} = 0.384 nm [8], making it suitable as a seed layer for the growth of LSMO films, as the lattice mismatch between the nanosheets and LSMO (a_{LSMO} = 0.386 nm) is -0.18 %. A very low lattice mismatch should mitigate issues caused by mechanical strain illustrated in Section 6.1.

The Si substrate with the NS layer was analysed by AFM before the deposition of LSMO. Selected images from the AFM scans are shown below in Figure 6.1. The AFM scans show frequent overlapping of the individual nanosheets near their edges. Occasional full overlap between two nanosheets was observed. From multiple AFM scans, it was determined that, on average, (91 ± 2) % of the substrate is covered by nanosheets. Additionally, average root mean square (RMS) roughness of (0.59 ± 0.04) nm was measured. The scans also revealed the presence of unknown agents randomly scattered throughout the surface. Ultrasonic cleaning with acetone and ethanol baths was attempted to rid the substrate of these impurities. This improved the situation slightly without damaging the NS seed layer.

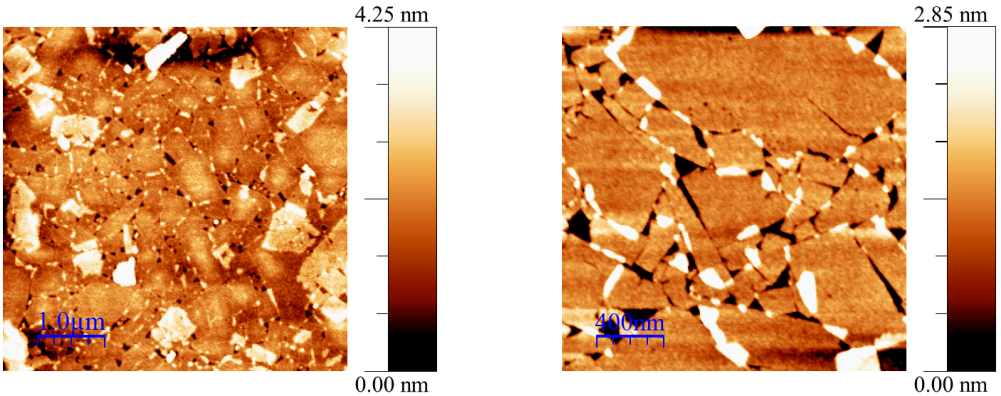

(a) NS/Si 5x5 µm^2 **(b)** NS/Si 2x2 µm^2

Figure 6.1 AFM tapping mode images of the nanosheet buffer layer at two levels of magnification.

6.3 LSMO/NS/Si thin films

Growing LSMO thin films on a CNO NS seed layer results in the growth of (001)-textured LSMO even on amorphous substrates [8]. (001)-textured growth was also observed in the case of the investigated samples where silicon was used as a substrate [9].

Growing LSMO on conventionally used single-crystal oxide substrates such as $SrTiO_3$ (STO) results in epitaxial growth, meaning the LSMO film grows as an extension of the substrate's crystalline structure. Epitaxial LSMO films are extensively studied, and their properties are well known [21], [32]. On the other hand, a polycrystalline film is made of small, randomly oriented crystal grains. This leads to the formation of magnetic domain walls at grain boundaries, which inhibit LSMO's transfer and magnetical properties [33]. A (001)-textured film grown on an NS seed layer comprises uniformly facing grains. The grains are oriented with their [001] crystallographic direction facing out of the plane of the samples' surface but are randomly rotated around the normal of the substrate.

6.4 Investigated LSMO/NS/Si films

The samples analysed in this work were deposited on a set of NS/Si substrates by a PLD set-up described in Section 4.1. The pulse repetition rate was 2 Hz, and the energy fluence of the KrF laser was 3 J/cm^2. The deposition was performed in a 110 mTorr oxygen atmosphere with the substrate kept at 650 °C. Post-deposition annealing was enacted at 75 Torr of background oxygen pressure. A series of samples with varying thicknesses were made by calculating the number of pulses required to grow a layer of the desired thickness. The target thicknesses of the films were 2, 5, 7, 10, 15, 40 and 100 nm.

The prepared samples were also analysed by AFM. An AFM scan of all samples is displayed in Figure 4.2. These scans revealed that the morphology of the deposited film copies the morphology of the NS layer. Dots on the AFM scans reveal a granular morphology of the surfaces of thicker samples. RMS roughness of the 2-15 nm films is in the (0.5 ± 0.1) nm range. The roughness then increased for the thicker films. The 40 nm sample has an RMS roughness of 1.5 nm, while the 100 nm sample has an RMS roughness of 1.8 nm. Both the granular structure of the films and the RMS roughness are in agreement with the behaviour observed in [8].

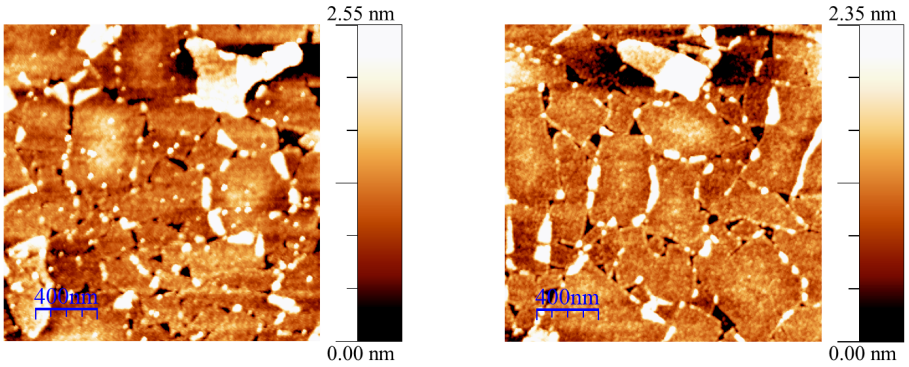

(a) 2 nm LSMO/NS/Si **(b)** 5 nm LSMO/NS/Si

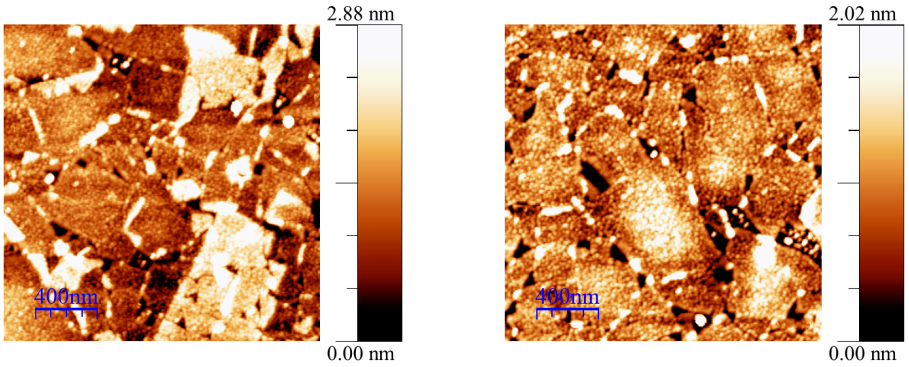

(c) 7 nm LSMO/NS/Si **(d)** 10 nm LSMO/NS/Si

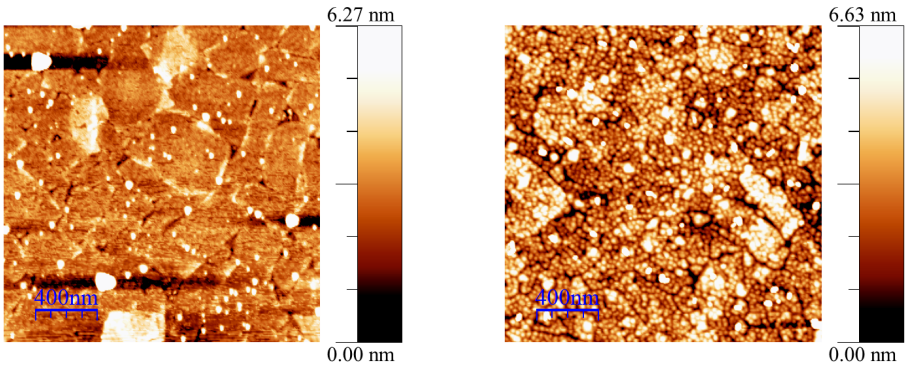

(e) 15 nm LSMO/NS/Si **(f)** 40 nm LSMO/NS/Si

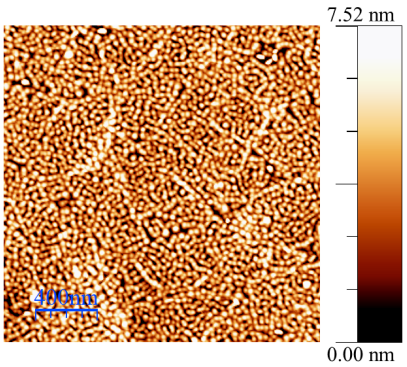

(g) 100 nm LSMO/NS/Si

Figure 6.2 AFM tapping mode images for all analysed samples.

Chapter 7

Permittivity tensor element spectra of investigated samples

Having introduced the theory, experimental techniques and the analysed samples, in this penultimate chapter, we present the culmination of this work's research efforts – information about the full permittivity tensor of LSMO thin films with varying thicknesses grown on NS/Si. First, the spectra of the diagonal permittivity tensor elements of all studied samples will be presented. Afterwards, the diagonal permittivity tensor element spectra and MO Kerr effect spectra will be used to numerically determine the spectra of the off-diagonal elements of the permittivity tensor.

7.1 Diagonal elements of the permittivity tensor

The spectra of the diagonal elements of the permittivity tensors were modelled from the ellipsometric angles measured by SE (see Figure 4.3) as a *B-Spline*. B-Spline, a shorthand for basis spline, is a smooth piecewise polynomial function. Its shape can be perfectly controlled by a defined number of control points, making them a good choice for curve-fitting and numerical differentiation. The samples were modelled as a series of 3 thin layers on a Si substrate. From the top, these were an LSMO layer, an NS+LSMO *effective medium approximation* (EMA) layer and a layer of SiO_2. EMA allows for including layers consisting of a mixture of materials while also accounting for the geometry of the mixture [34]. In this work, EMA was used to factor in the presence of LSMO between individual nanosheets. A 10% LSMO content in the NS seed layer and a depolarisation factor of 0 representing inclusions parallel to the surface was assumed based on the AFM scans. The modelling process was carried out using the *CompleteEASE* software.

The thicknesses of the NS+LSMO EMA and SiO_2 layers were approximated from SE measurements conducted first on the pure Si substrate itself and afterwards on the NS/Si substrate. From these measurements, it was determined that the SiO_2 layer is around 4.5 nm, while the NS layer is around 2.3 nm. The optical constants of Si and SiO_2 were taken from [35]. The spectra of their respective permittivities can be found in Appendix A.1 along with the permittivity spectra of the NS.

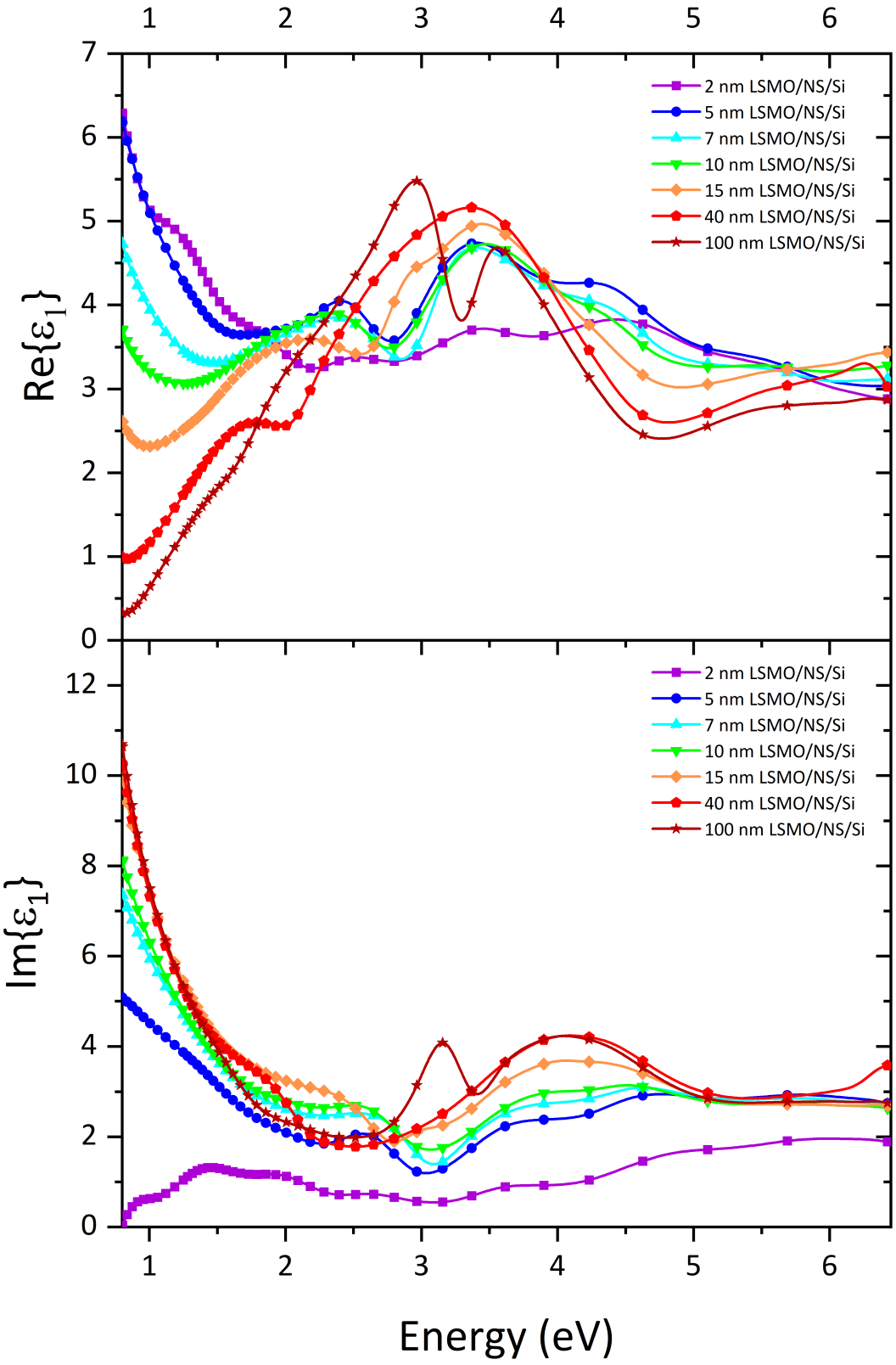

Figure 7.1 Real and imaginary parts of the diagonal elements of the permittivity tensor of LSMO thin films with varying thicknesses grown on an NS/Si substrate.

The spectra of the diagonal permittivity tensor elements of all analysed samples are presented in Figure 7.1. The calculated optical constants conform to the Kramers-Kronig relations. Analysis of the spectra of the imaginary parts (bottom panel of Figure 7.1) reveals several trends. The position of local maxima present in the imaginary part spectra corresponds to an electronic transition of the same energy. First, a gradual red-shift of the absorption structure, and hence the electronic transition, located outside the measurement bounds in the infrared region, can be observed. The energy of these infrared electron transitions decreases as the thickness of the LSMO film increases. This hints at a continuous relaxation of strain within the layer as the film grows in thickness since such a shift in the energy levels along with decreasing strain would be consistent with the behaviour observed in [21]. There also seem to be two more electron transitions in the 3.5 eV to 4.5 eV energy range, which is again in agreement with [21]. These transitions move closer together with increasing layer thickness until they are not recognisable at a glance. This phenomenon can also be attributed to strain relaxation. Strain in the thinner layers induces modifications in the crystalline structure of LSMO, which result in higher energy differences between different energy levels of the manganese atom. As the strain relaxes, these energy levels move closer together, bringing forth the behaviour observed in Figure 7.1. The 100 nm sample exhibits an extra peak near 3 eV, which is not visible in the spectra of other samples. It is plausible this peak forms as an extension of the effect observable between 2–3 eV for the other samples, but the origin of this effect is not known.

Further insight into the electronic structure of all samples could be gained by fitting the imaginary parts of the diagonal permittivity tensor elements by Lorentz curves. This would reveal the positions and number of electronic transitions present for each layer, which is necessary information to draw further conclusions about the electronic structure of analysed samples. However, this lies outside the scope of this work.

7.2 MO Kerr effect

MOKE spectra were measured first on the set-up depicted in Figure 4.4. The measurements were realised at nearly normal light incidence in a polar configuration with the magnetic field set to 1 T and at room temperature.

The recorded MOKE spectra are shown in Figure 7.2. There we can see that the intensity of the MO signal and shape of the MOKE spectra is heavily dependent on thickness of the LSMO film. The thinner films, namely the 7, 10 and 15 nm samples, give MOKE spectra similar to those recorded for LSMO films on STO [21]. On the other hand, a very faint MO signal was recorded even from the 2 nm thick sample. This is intriguing when compared to the behaviour observed in [36], where it was found that approximately the first six monolayers ($\sim$ 2 nm) of LSMO grown on STO are magnetically inert due to an interplay of mechanical strain and interface effects suppressing the DE mechanism. This hints at ferromagnetic ordering taking place from a lower number of monolayers owing to lower lattice mismatch.

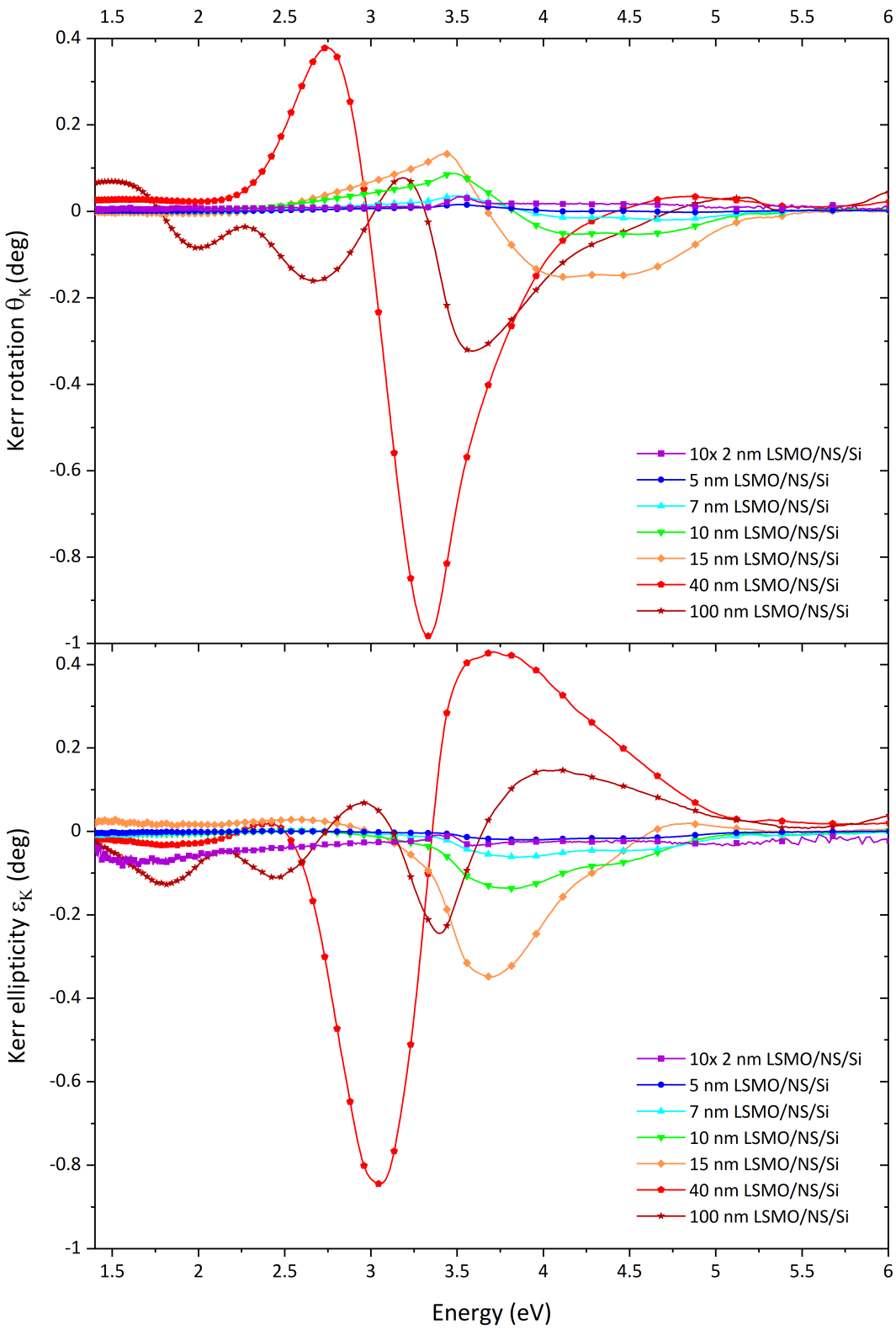

Figure 7.2 Kerr rotation and Kerr ellipticity of LSMO thin films with varying thicknesses grown on an NS/Si substrate. Data corresponding to the 2 nm LSMO film were multiplied tenfold for better readability.

The 40 nm LSMO film had the largest recorded MOKE from all the samples. A supplementary reflectometry measurement conducted on it revealed very low reflectivity of the sample (< 10 %) in the 2.4-3.4 eV energy range. Looking at the definition of MOKE 2.43, one can deduce that a small value of r_{ss} would explain the unusually large magnitude of Kerr rotation and Kerr ellipticity.

The closest published comparison to the MOKE spectra of the 100 nm sample we found is in [37], where they analyse a 100 nm LSMO film grown on $LaAlO_3$ (LAO). From [37], we see that the magnitude of the recorded MOKE is comparable to that of the film grown on LAO. LSMO on LAO grows under considerable compressive strain due to its lattice mismatch of $m = 2.27$ %, which leads to a degradation of LSMO's magnetical properties. However, at a film thickness of 100 nm this strain is partially relaxed, explaining the similarity in magnitude of the recorded MO response between LSMO/LAO and the investigated samples.

7.3 Off-diagonal elements of the permittivity tensor

The spectra of the off-diagonal elements of the permittivity tensor of all but the 100 nm sample were numerically determined by the process illustrated in 3.2. The algorithm didn't converge in the case of the 100 nm sample. The suspected cause of this behaviour is incident light not being able to interact with the whole of the used multi-layer model due to non-negligible absorption in some parts of the visible light spectrum. The absorption coefficient spectrum of the 100 nm sample is included in appendix A.2. The Kerr spectra of the 100 nm sample were accurately simulated by Yeh formalism using ε_2 spectra of the 40 nm sample (presented in appendix A.3). This means there is little difference in the ε_2 spectra between the 40 nm and 100 nm samples. The ε_2 spectra of the 100 nm sample were approximated by the bulk formula. The bulk formula describes the MO response of a semi-infinite material, and its derivation can be found in [14].

The spectra of the off-diagonal permittivity tensor element of all samples are presented in Figure 7.3. There we can see that the magnitude of the spectra generally increases with film thickness. This can be attributed to gradual strain relaxation enabling stronger ferromagnetic ordering as the film grows in thickness. The main feature of all the spectra is the spectroscopic structure (a peak in the real part and an S shape in the imaginary part) around 3.6 eV. This feature has been shown in literature to correspond to an already reported electronic transition from the O $2p$ state into the Mn t_{2g} states. Its presence has been reported for bulk LSMO [38], films grown on single-crystal substrates [39], [37], as well as NS/Si [40]. A neighbouring spectroscopic structure manifested as a peak in the imaginary part of the ε_2 spectra of the thinner films at around 3.25 eV. This peak and the peak located at around 3.5 eV merge together in the spectra of the 40 nm and 100 nm samples. Such behaviour abides by the established motif of strain in the thinner layers inducing larger splitting of energy levels of the manganese ion via the deformation of the oxygen octahedra. As the strain relaxes in the thicker films, these split energy levels move closer together, making them mutually unrecognisable. We can see a similar effect happening with the peak sitting at around 2.25 eV in the imaginary part of the ε_2 spectra.

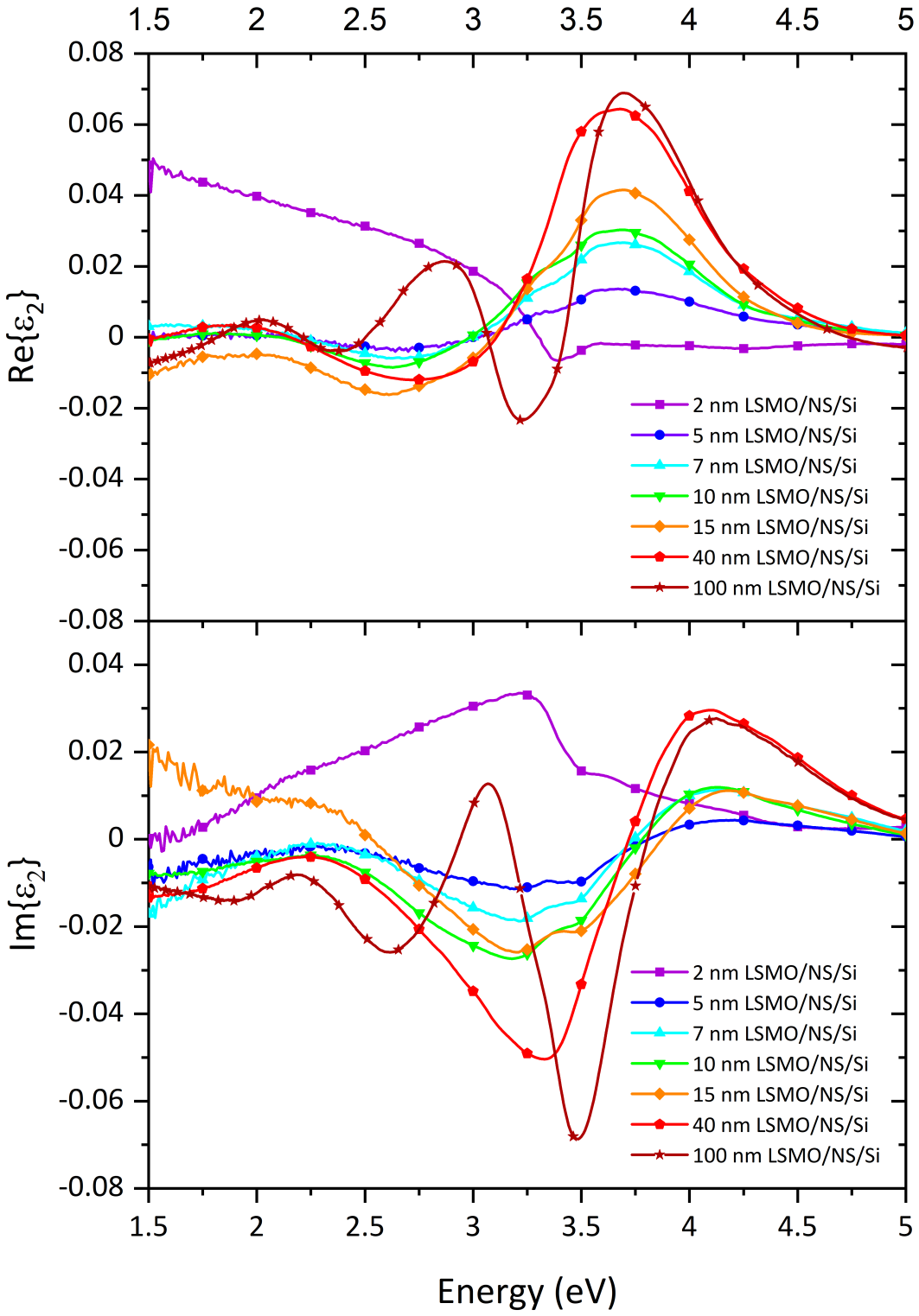

Figure 7.3 Real and imaginary parts of the off-diagonal elements of the permittivity tensor of LSMO thin films with varying thicknesses grown on an NS/Si substrate.

The 2 nm sample is a clear outlier in the series. Judging by its very weak MO response and these spectra, it seems the 2 nm sample has its Curie temperature near room temperature. The Curie temperature of LSMO films is known to decrease with increasing strain [41], and the spectra show a clear trend of thinner layers experiencing larger strain.

The spectra of the 100 nm sample show an extra spectroscopic structure centred at 3 eV. This structure is also visible in the spectra of the diagonal elements of the permittivity tensor in Figure 7.1 and the MOKE spectra in Figure 7.2. It is important to note, that the absorption coefficient of the 100 nm sample (See Appendix A.2) decreases to less than half its UV value for photon energies less than 3.5 eV. Hence the bulk formula is a worse approximation for lower photon energies and can produce unnatural artefacts in the infrared part of the spectrum.

Conclusion

The thickness-dependent development of optical and magneto-optical properties of LSMO films grown on an NS/Si substrate was analysed using SE and MO spectroscopy. The off-diagonal elements of the samples' permittivity tensors were then numerically determined from the acquired data. The series of investigated samples showed gradual strain relaxation with increasing layer thickness, which was observable as systematic changes to known electronic transitions of LSMO.

The most notable effect observed was the splitting of peaks in the permittivity tensor element spectra of the thinner samples. This can be explained by the larger strain within the thinner films causing more pronounced defects in the crystalline structure. The deformation of the crystalline structure leads to a larger splitting of the energy levels in the electronic structure of LSMO, which manifests itself as a bigger number of observable electronic transitions in the permittivity tensor element spectra. This occurs due to a lowering of the symmetry of the oxygen octahedra and concurrent lifting of the degeneracy of the electron energy levels in the manganese ion. A steady increase in the magnitude of the off-diagonal element of the permittivity tensor spectra with increasing film thickness was also recorded. The increasing MO effect of the samples as they grow in thickness can also be attributed to strain relaxation and better crystalline growth, as strain and bad crystalline quality inhibit the double-exchange interaction responsible for the ferromagnetic ordering in LSMO.

A set of textured high-quality LSMO films was successfully grown on a silicon substrate with a CNO seed layer. The LSMO/NS/Si thin films exhibit optical and magneto-optical properties comparable to LSMO films grown on STO. A faint MO response was recorded from our 2 nm sample, which could hint at ferromagnetic ordering taking place at lower thicknesses than was observed for films grown on STO. This could be explained by the lower lattice mismatch between LSMO and CNO inducing lower strain in the grown films.

A more thorough examination of the electronic structure and temperature-based measurements are planned in order to gain further insight into the formation of optical and magneto-optical of LSMO/NS/Si thin films.

Bibliography

[1]R. von Helmolt, J. Wecker, B. Holzapfel, L. Schultz, and K. Samwer, "Giant negative magnetoresistance in perovskitelike $La_{2/3}Ba_{1/3}MnO_x$ ferromagnetic films", Phys. Rev. Lett. **71**, 2331–2333 (1993).

[2]G. Jonker and J. V. Santen, "Ferromagnetic compounds of manganese with perovskite structure", Physica **16**, 337–349 (1950).

[3]M. Bowen, M. Bibes, A. Barthélémy, J.-P. Contour, A. Anane, Y. Lemaıtre, and A. Fert, "Nearly total spin polarization in $La_{2/3}Sr_{1/3}MnO_3$ from tunneling experiments", Applied Physics Letters **82**, 233–235 (2003).

[4]O. Rousseau, S. Flament, B. Guillet, M. L. C. Sing, and L. Méchin, "Magnetic sensors based on AMR effect in LSMO thin films", Proceedings (American Bar Association. Section of International and Comparative Law) **1**, 635 (2017).

[5]H. Jalili, J. W. Han, Y. Kuru, Z. Cai, and B. Yildiz, "New insights into the strain coupling to surface chemistry, electronic structure, and reactivity of $La_{2/3}Sr_{1/3}MnO_3$", The Journal of Physical Chemistry Letters **2**, 801–807 (2011).

[6]C. Zener, "Interaction between the d-shells in the transition metals. II. ferromagnetic compounds of manganese with perovskite structure", Phys. Rev. **82**, 403–405 (1951).

[7]J. M. Rondinelli, S. J. May, and J. W. Freeland, "Control of octahedral connectivity in perovskite oxide heterostructures: an emerging route to multifunctional materials discovery", MRS Bulletin **37**, 261–270 (2012).

[8]A. Boileau, M. Dallocchio, F. Baudouin, A. David, U. Lüders, B. Mercey, A. Pautrat, V. Demange, M. Guilloux-Viry, W. Prellier, and A. Fouchet, "Textured manganite films anywhere", ACS Applied Materials & Interfaces, acsami.9b12209 (2019).

[9]T. Maleček, M. Thomas, G. Agnus, L. Horák, A. Melzer, P. Lecoeur, and M. Veis, "Magnetic, optical and magneto-optical properties of strain-free $La_{2/3}Sr_{1/3}MnO_3$ on si substrates with $Ca_2Nb_3O_{10}$ nanosheet seed layer", [Poster presentation], MMM 2022, 2022.

[10]J. D. Jackson, *Classical electrodynamics*, 3rd ed (Wiley, 1999).

[11]L. Landau, *Electrodynamics of continuous media*, 2nd ed., Vol. Volume 8 (Pergamon, 1984).

[12]H. S. Bennett and E. A. Stern, "Faraday effect in solids", Physical Review (Series I) **137**, A448–A461 (1965).

[13]B. Max and W. Emil, *Principles of optics*, 7th (Cambridge University Press, 1999).

[14]M. Nývlt, “Optical interactions in ultrathin magnetic film structures”, PhD thesis (Charles University, 1996).

[15]Štefan Višňovský, *Optics in magnetic multilayers and nanostructures* (CRC Press, 2006).

[16]P. Yeh, “Optics of anisotropic layered media: a new 4 x 4 matrix algebra”, Surface Science Letters **96**, 10.1016/0167-2584(80)90034-1 (1980).

[17]D. P. Norton, “Pulsed laser deposition of complex materials: progress toward applications”, in *Pulsed laser deposition of thin films* (John Wiley & Sons, Ltd, 2006) Chap. 1, pp. 1–31.

[18]W Prellier, P. Lecoeur, and B Mercey, “Colossal-magnetoresistive manganite thin films”, Journal of Physics Condensed Matter **13**, R915–R944 (2001).

[19]Q. Zhong, D. Inniss, K. Kjoller, and V. Elings, “Fractured polymer/silica fiber surface studied by tapping mode atomic force microscopy”, Surface Science Letters **290**, 10.1016/0167-2584(93)90906-y (1993).

[20]R. M. Azzam, N. M. Bashara, and S. S. Ballard, “Ellipsometry and polarized light”, Physics Today (1978).

[21]M. Zahradník, “Dynamic control of magnetization for spintronic applications studied by magneto-optical methods”, PhD thesis (Charles University, 2019).

[22]A.-M. Haghiri-Gosnet and J.-P. Renard, “CMR manganites: physics, thin films and devices”, Journal of Physics D: Applied Physics **36**, R127 (2003).

[23]A. Vailionis, H. Boschker, W. Siemons, E. P. Houwman, D. H. A. Blank, G. Rijnders, and G. Koster, “Misfit strain accommodation in epitaxial perovskites: lattice rotations and lattice modulations”, Physical Review B **83**, 10.1103/physrevb.83.064101 (2011).

[24]J. M. D. Coey, *Magnetism and magnetic materials* (Cambridge University Press, 2010).

[25]J. V. Santen and G. Jonker, “Electrical conductivity of ferromagnetic compounds of manganese with perovskite structure”, Physica **16**, 599–600 (1950).

[26]J. B. Goodenough, “Theory of the role of covalence in the perovskite-type manganites $[\mathrm{La}, M(\mathrm{II})]\mathrm{MnO}_3$”, Phys. Rev. **100**, 564–573 (1955).

[27]A. Tebano, A. Orsini, P. G. Medaglia, D. Di Castro, G. Balestrino, B. Freelon, A. Bostwick, Y. J. Chang, G. Gaines, E. Rotenberg, and N. L. Saini, “Preferential occupation of interface bands in $\mathrm{La}_{2/3}\mathrm{Sr}_{1/3}\mathrm{MnO}_3$ films as seen via angle-resolved photoemission”, Phys. Rev. B **82**, 214407 (2010).

[28]A. Khapikov, L. Uspenskaya, I. Bdikin, Y. Mukovskii, S. Karabashev, D. Shulyaev, and A. Arsenov, “Magnetic domains and twin structure of the $\mathrm{La}_{2/3}\mathrm{Ba}_{1/3}\mathrm{MnO}_3$ single crystal”, Applied Physics Letters **77**, 2376–2378 (2000).

[29]F. Tsui, M. C. Smoak, T. K. Nath, and C. B. Eom, “Strain-dependent magnetic phase diagram of epitaxial $\mathrm{La}_{0.67}\mathrm{Sr}_{0.33}\mathrm{MnO}_3$ thin films”, Applied Physics Letters **76**, 2421–2423 (2000).

[30]I. Bergenti, V. Dediu, E. Arisi, M. Cavallini, F. Biscarini, C. Taliani, M. de Jong, C. Dennis, J. Gregg, M. Solzi, and M. Natali, “Spin polarized $\mathrm{La}_{0.7}\mathrm{Sr}_{0.3}\mathrm{MnO}_3$ thin films on silicon”, Journal of Magnetism and Magnetic Materials **312**, 453–457 (2007).

[31]T. TOKUMITSU, K. TODA, T. AOYAGI, D. SAKURABA, K. UEMATSU, and M. SATO, "Powder neutron diffraction study of layered perovskite, $KCa_2Nb_3O_{10}$", Journal of the Ceramic Society of Japan **114**, 795–797 (2006).

[32]M. Španková, V. Štrbík, E. Dobročka, Chromik, M. Sojková, D. Zheng, and J. Li, "Characterization of epitaxial LSMO thin films with high curie temperature prepared on different substrates", Vacuum **126**, 24–28 (2016).

[33]S. Yang, W. Kuang, Y. Liou, W. Tse, S. Lee, and Y. Yao, "Growth and characterization of $La_{2/3}Sr_{1/3}MnO_3$ films on various substrates", Journal of Magnetism and Magnetic Materials **268**, 326–331 (2004).

[34]J. Hilfiker, *Modeling nanostructures with a graded anisotropic EMA*, Ellipsometer manual, 2007.

[35]C. M. Herzinger, B. Johs, W. A. McGahan, J. A. Woollam, and W. Paulson, "Ellipsometric determination of optical constants for silicon and thermally grown silicon dioxide via a multi-sample, multi-wavelength, multi-angle investigation", Journal of Applied Physics **83**, 3323–3336 (1998).

[36]M Veis, M Zahradnik, R Antos, S Visnovsky, P. Lecoeur, D Esteve, S Autier-Laurent, J.-P. Renard, and P Beauvillain, "Interface effects and the evolution of ferromagnetism in $La_{2/3}Sr_{1/3}MnO_3$ ultrathin films", Science and Technology of Advanced Materials **15**, 015001 (2013).

[37]H. L. Liu, K. S. Lu, M. X. Kuo, L. Uba, S. Uba, L. M. Wang, and H.-T. Jeng, "Magneto-optical properties of $La_{0.7}Sr_{0.3}MnO_3$ thin films with perpendicular magnetic anisotropy", Journal of Applied Physics **99**, 043908, 10.1063/1.2173681 (2006).

[38]S. Yamaguchi, Y. Okimoto, K. Ishibashi, and Y. Tokura, "Magneto-optical kerr effects in perovskite-type transition-metal oxides: $La_{1-x}Sr_xMnO_3$ and $La_{1-x}Sr_xCoO_3$", Phys. Rev. B **58**, 6862–6870 (1998).

[39]M. Zahradník, T. Maroutian, M. Zelený, L. Horák, G. Kurij, T. Maleček, L. Beran, Višňovský, G. Agnus, P. Lecoeur, and M. Veis, "Electronic structure of $La_{2/3}Sr_{1/3}MnO_3$: interplay of oxygen octahedra rotations and epitaxial strain", Phys. Rev. B **99**, 195138 (2019).

[40]T. Maleček, "Substrátem kontrolované fyzikální vlastnosti tenkých vrstev magnetických oxidů pro spintronické aplikace", Diploma thesis (Charles University, 2022).

[41]T. Maleček, "Vliv pnutí na magnetooptické vlasnosti $La_{2/3}Sr_{1/3}MnO_3$", Bachelor thesis (Charles University, 2020).

List of Figures

2.1 The ellipse of polarisation. 9
2.2 Reflected and transmitted wave with their respective coordinate systems. 12

3.1 Definitions of polar, longitudinal and transverse geometries for MOKE measurements. 18
3.2 Diagram of a multi-layer anisotropic sample used in the Yeh formalism derivation. 20

4.1 A pulsed laser deposition (PLD) set-up schematic. 26
4.2 An atomic force microscopy (AFM) set-up schematic. 27
4.3 A rotating compensator ellipsometry (RCE) set-up schematic. . . . 28
4.4 A rotating analyser magneto-optical spectroscopy set-up schematic. 30

5.1 Ideal structure of a cubic pervskite of type ABO_3. 32
5.2 The hysteresis loop of a ferromagnetic material. 34
5.3 The double-exchange (DE) interaction in LSMO. 35

6.1 AFM tapping mode images of CNO nanosheets. 37
6.2 AFM tapping mode images of all analysed samples. 39

7.1 Diagonal permittivity tensor element spectra of all analysed samples. 41
7.2 The magneto-optical Kerr effect (MOKE) spectra for all analysed samples. 43
7.3 Off-diagonal permittivity tensor element spectra of all analysed samples. 45

A.1 Optical constants of Si. 53
A.2 Optical constants of native SiO_2. 54
A.3 Optical constants of the CNO nanosheet layer. 54
A.4 The absorption coefficient spectrum of the 100 nm LSMO/NS/Si sample. 55
A.5 Simulated MOKE of the 100 nm LSMO/NS/Si sample using ε_2 spectra of the 40 nm sample 56

List of Abbreviations

AFM	-	atomic force microscopy
CNO	-	$Ca_2Nb_3O_{10}$
DE	-	double-exchange
EMA	-	effective medium approximation
KCNO	-	$KCa_2Nb_3O_{10}$
LAO	-	$LaAlO_3$
LSMO	-	$La_{2/3}Sr_{1/3}MnO_3$
MO	-	magneto-optical
MOKE	-	magneto-optical Kerr effect
NS	-	nanosheet
PLD	-	pulsed laser deposition
RAE	-	rotating analyser ellipsometry
RCE	-	rotating compensator ellipsometry
RMS	-	root mean square
SE	-	spectroscopic ellipsometry
STO	-	$SrTiO_3$

Appendix A

Supplementary graphs

A.1 Diagonal elements of the permittivity tensors of selected materials

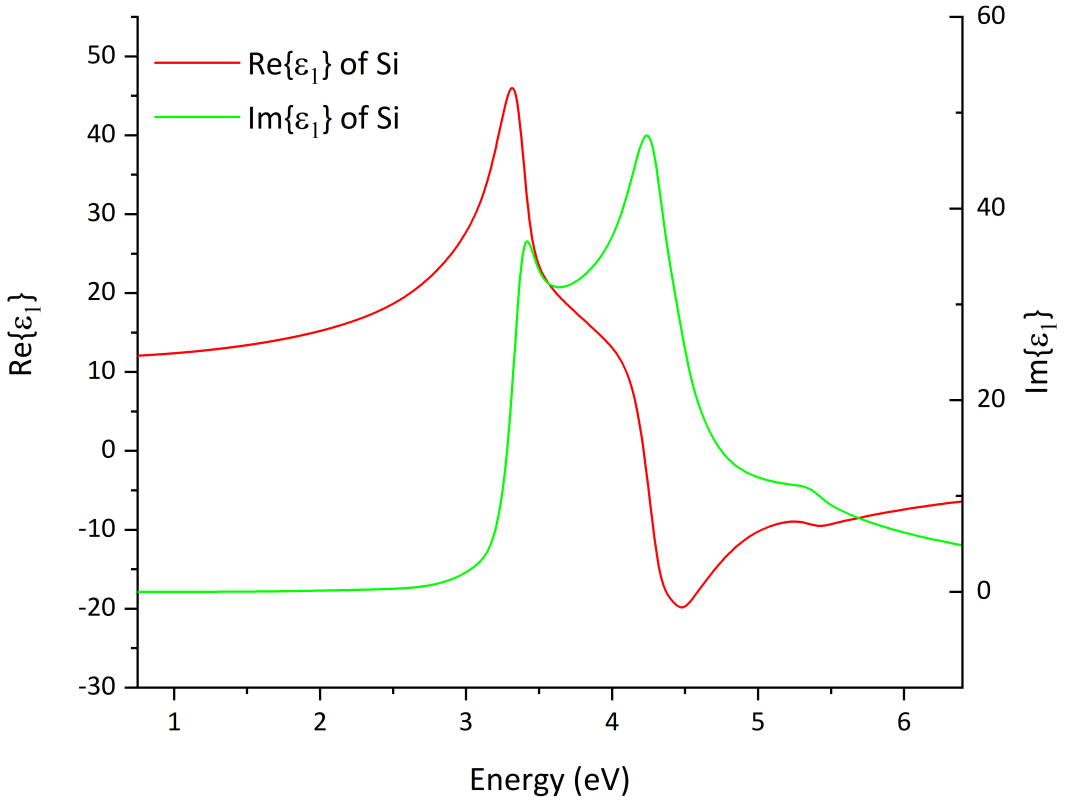

Figure A.1 Optical constants of Si used for modelling our samples. Data taken from [35].

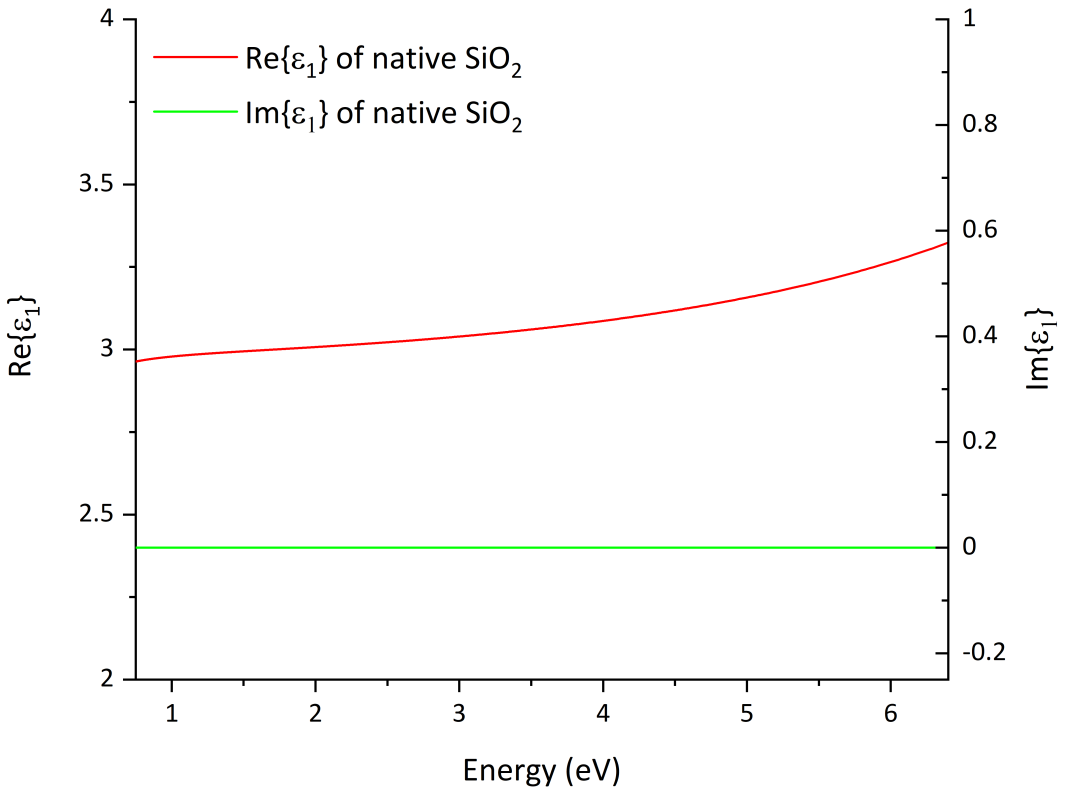

Figure A.2 Optical constants of native SiO_2 used for modelling our samples. Data taken from [35].

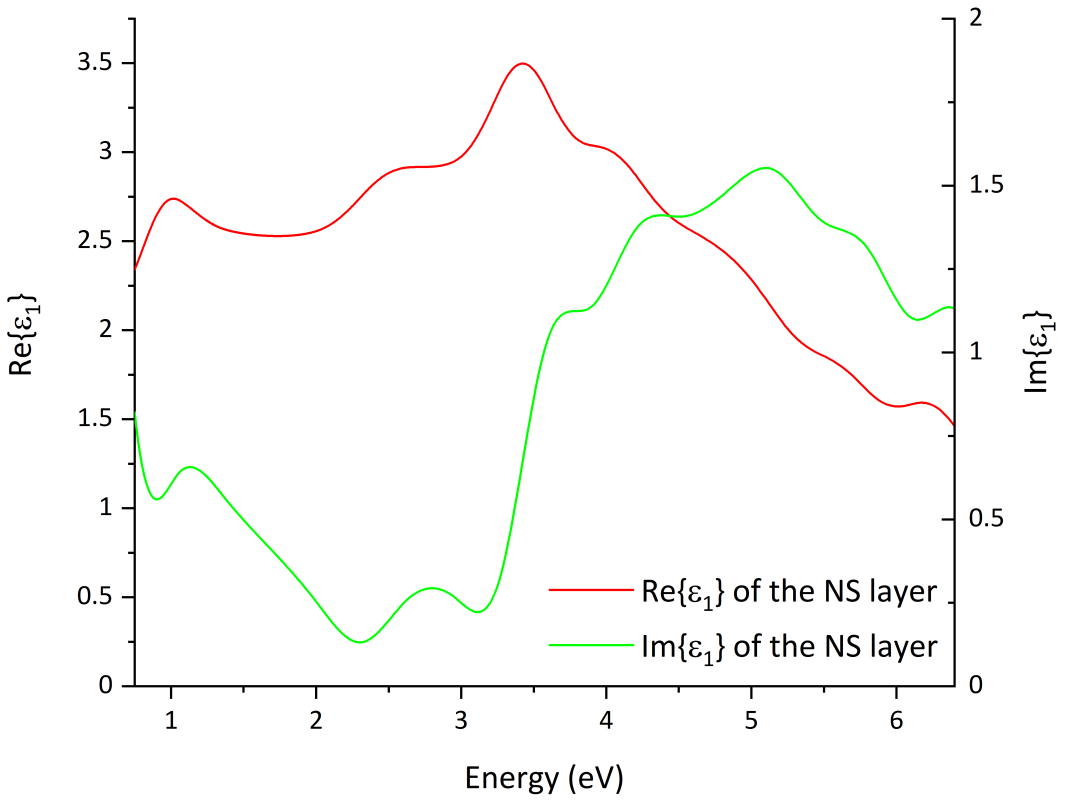

Figure A.3 Optical constants of the CNO nanosheet buffer layer.

A.2 100 nm LSMO/NS/Si absorption coefficient

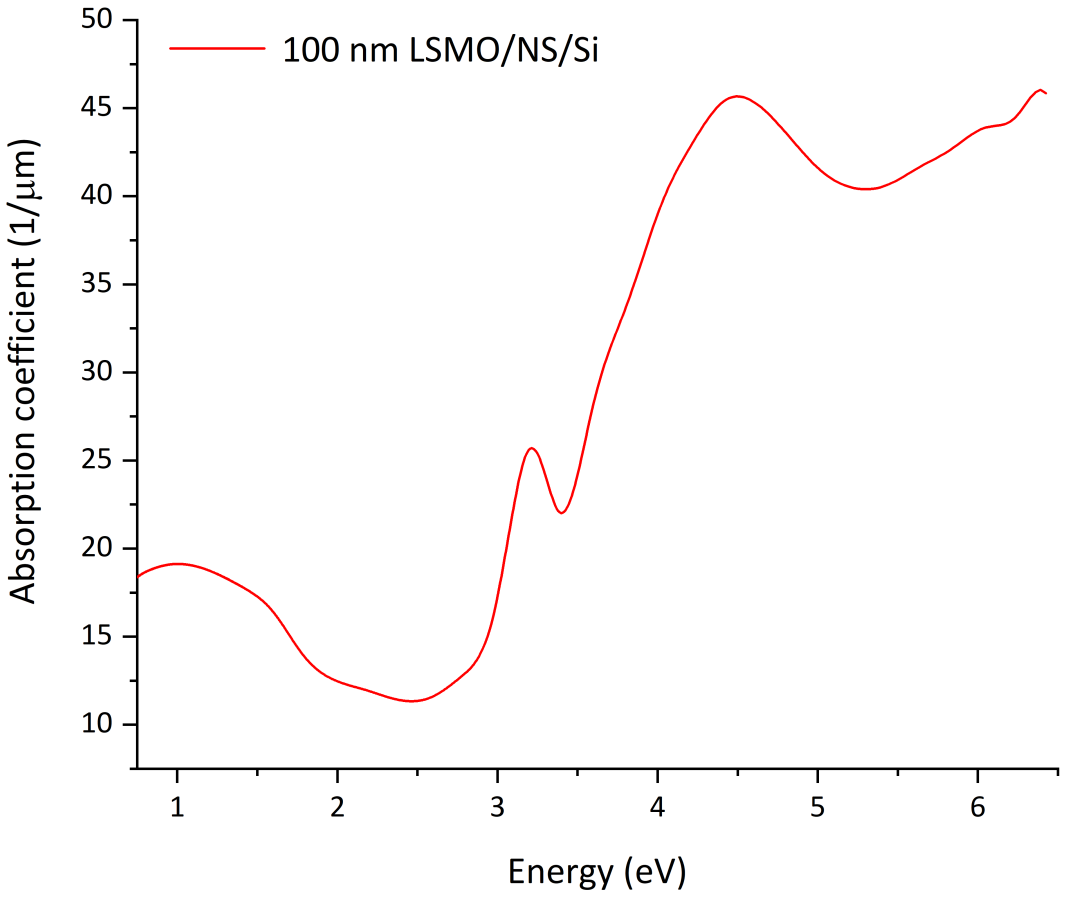

Figure A.4 The absorption coefficient spectrum of the 100 nm LSMO/NS/Si sample.

A.3 Simulated MOKE of the 100 nm sample

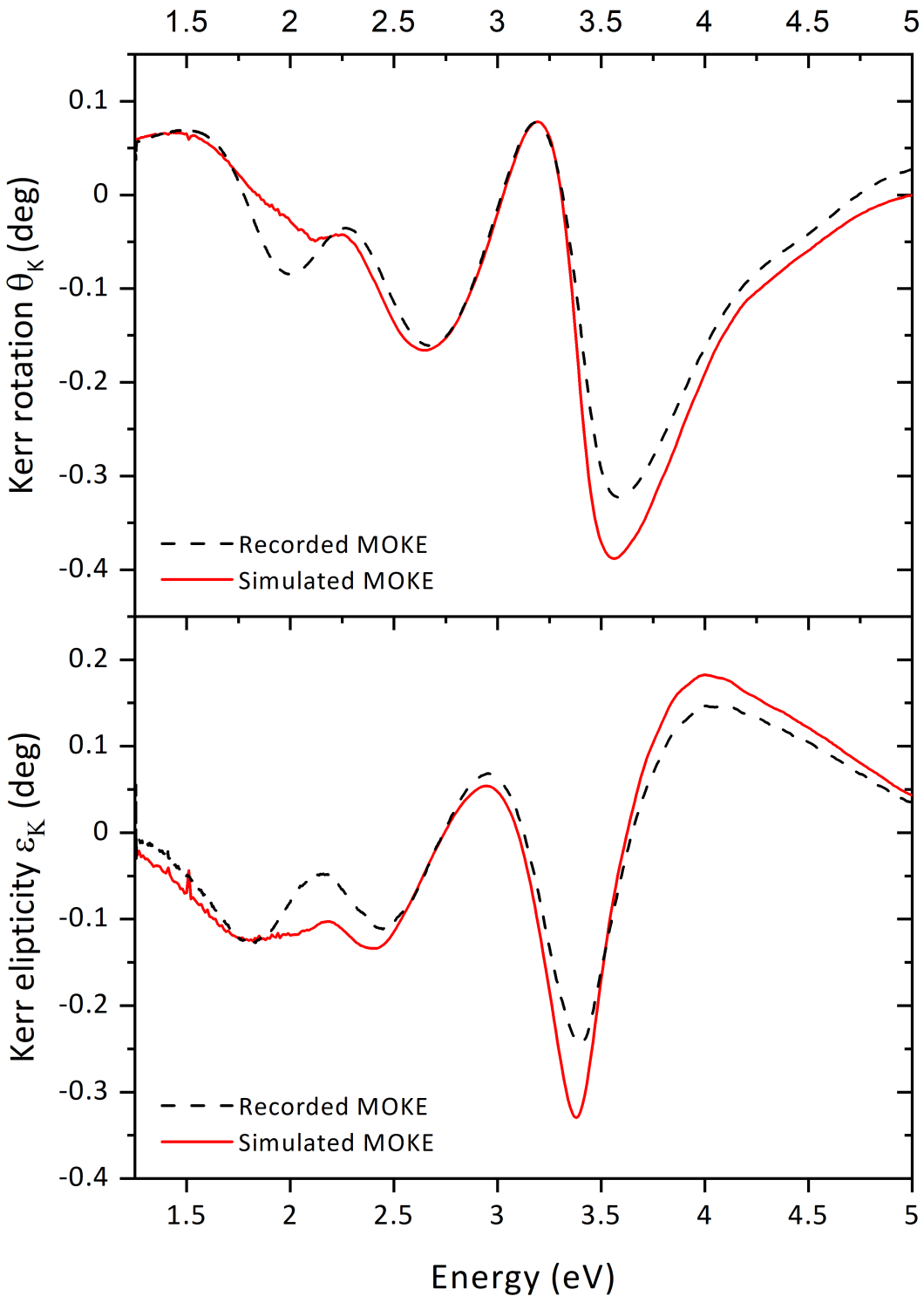

Figure A.5 The recorded MOKE spectrum of the 100 nm sample and the MOKE spectrum simulated from ε_2 spectra of the 40 nm sample using Yeh formalism.